

Anti-trypanosomal quinazolines targeting lysyl-tRNA synthetases show partial efficacy in a mouse model of acute Chagas disease

Lindsay B. Tulloch^{1,§}, Hugh Tawell^{2,§}, Annie E Taylor³, Marta Lopes Lima¹, Alice Dawson⁴, Sandra Carvalho¹, Richard J. Wall^{1,†}, Victoriano Corpas-Lopez¹, Gourav Dey¹, Jack Duggan¹, Luma Godoy Magalhaes⁴, Leah S. Torrie⁴, Laura Frame⁴, David Robinson⁴, Stephen Patterson¹, Michele Tinti¹, George W Weaver², William J Robinson³, Monica Cal^{5,6}, Marcel Kaiser^{5,6}, Pascal Mäser^{5,6}, Peter Sjö⁷, Benjamin Perry^{7,‡}, John M. Kelly⁸, Amanda Fortes Francisco⁸, Avninder S. Bhambra^{3,*}, Susan Wyllie^{1,*}

Affiliations:

¹Wellcome Centre for Anti-Infectives Research, School of Life Sciences, University of Dundee, Dundee, UK.

²Department of Chemistry, Loughborough University, Loughborough, LE11 3TU, UK.

³Leicester School of Allied Health Sciences, De Montfort University, The Gateway, Leicester, LE1 9BH, UK.

⁴Drug Discovery Unit, School of Life Sciences, University of Dundee, Dundee, UK.

⁵Swiss Tropical and Public Health Institute, 4123 Allschwil, Switzerland.

⁶University of Basel, 4003 Basel, Switzerland.

⁷Drugs for Neglected Diseases initiative (DNDi), 1202 Geneva, Switzerland.

⁸London School of Hygiene and Tropical Medicine, London, UK.

†Current address: London School of Hygiene and Tropical Medicine, London, UK.

‡Current address: Medicxi, Geneve 1204, Switzerland

§Authors contributed equally.

*Corresponding author Emails: s.wyllie@dundee.ac.uk; abhambra@dmu.ac.uk.

One Sentence Summary:

Quinazolines targeting lysyl tRNA synthase show partial efficacy in a mouse model of Chagas disease

Accessible Summary:

New drugs are required to treat Chagas disease, a deadly parasitic infection prevalent in Latin America. Here, Tulloch et al. investigate the mechanism of action of a new series of quinazoline compounds demonstrating potential against *Trypanosoma cruzi*, the causative agent of Chagas disease. Genetic, biochemical and proteomics approaches identify the molecular target of these compounds as lysyl-tRNA-synthetase-1. The lead compound from the series is partially efficacious in a model of acute Chagas disease thus identifying *T. cruzi* lysyl-tRNA-synthetase-1 as a viable drug target. However, this quinazoline series will require further development to become a future treatment for this neglected disease.

Abstract

The protozoan parasite *Trypanosoma cruzi* causes Chagas disease, which is among the deadliest parasitic infections in Latin America. Current therapies are toxic and lack efficacy against chronic stage infection thus new drugs are urgently required. Here, we describe a new series of quinazoline compounds with potential against *T. cruzi* and the related trypanosomatids *T. brucei* and *Leishmania donovani* *in vitro*. We demonstrate partial efficacy of a lead quinazoline compound in a mouse model of acute Chagas disease. We conducted mechanism of action studies using several orthogonal approaches and confirmed that this new quinazoline compound series targeted the

47 ATP-binding pocket of lysyl-tRNA synthetase 1 (KRS1) in *T. cruzi*. A high-resolution crystal
48 structure of KRS1 bound to the drug indicated binding interactions that led to KRS1 inhibition.
49 Our study identifies KRS1 as a druggable target for treating *T. cruzi* infection. This quinazoline
50 series shows potential for treating Chagas disease but will require further development to become
51 a future treatment for this neglected disease.

INTRODUCTION

Chagas disease, caused by infection with the protozoan parasite *Trypanosoma cruzi*, is responsible for more fatalities than any other parasitic disease in Latin America and is a leading cause of infectious cardiomyopathy worldwide (1). Chagas disease cases in the USA and Europe are on the rise, driven predominantly by migration from endemic countries (2, 3). However, it should be noted that global warming is driving a shift in the geographical range of the Chagas disease vector, bugs of the Reduviidae family, raising the possibility that an increasing number of countries may experience endemic transmission (4). An estimated 6-7 million people are infected with *T. cruzi* and a further 75 million people are at risk of infection (www.who.int) (3). Approximately 30% of infected individuals progress to chronic, symptomatic disease that commonly affects the cardiovascular and digestive systems causing cardiomyopathy or digestive tract megasyndromes (5). Both forms of the disease are associated with major morbidity and mortality. At present, only two drugs, benznidazole and nifurtimox, are approved for the treatment of Chagas disease. Both are nitroheterocyclic prodrugs that require reduction catalyzed by a type I nitroreductase (NTR1) for biological activity (6-8). These drugs are associated with toxic side-effects that are often so severe that they prevent patients from completing treatment regimens (9, 10). In addition, both drugs are less efficacious in the chronic stage of the disease, the stage in which the vast majority of patients are diagnosed. Thus, new therapeutics with improved efficacy and reduced toxicity are urgently required.

Anti-chagasic drug discovery has long been hampered by a lack of dedicated resources. The most recent clinical trials have focused on assessing drugs repurposed from other disease indications rather than new chemical entities optimized for Chagas disease. To date, this strategy has proven ineffective. Most notably, the anti-fungal drug posaconazole that targets C14 α sterol

demethylase (CYP51), a key enzyme in the sterol biosynthetic pathway, failed in phase II clinical trials, with the vast majority of patients relapsing within a year of treatment (11). This was despite preliminary data indicating promising *in vitro* potency and *in vivo* efficacy in murine models of infection (12, 13). Similarly, the nitroimidazole fexinidazole, an oral drug currently used in the treatment of human African trypanosomiasis (14), proved ineffective in phase II proof-of-concept trials for Chagas disease. The clinical failure of both drugs has been partially attributed to their inability to eradicate persister forms of *T. cruzi* with reduced cell proliferation rates (15-17). Collectively, these studies emphasize the need for dedicated Chagas disease drug discovery programs aimed at delivering compounds capable of killing all developmental forms of this parasite at all stages of disease.

Here, we describe our orthogonal genetic, molecular, and biochemical studies to determine the molecular target of a quinazoline series of compounds demonstrating promising anti-chagasic activity. Screening of this series against the intracellular amastigote form of *T. cruzi*, identified hits that demonstrated *in vitro* potency superior to the current standard of care benznidazole and with limited mammalian cell cytotoxicity. Two compounds (DMU371 and DMU759) from this series were subjected to comprehensive drug target deconvolution studies leading to the identification of *T. cruzi* lysyl-tRNA synthetase (*TcKRS1*) as the molecular target of both quinazolines. Most notably, proof-of-concept studies in a murine model of acute Chagas disease demonstrated that DMU579 was capable of reducing parasitemia by up to 81%. Collectively, these studies identified KRS1 as a chemically validated drug target for the treatment of *T. cruzi* infection.

RESULTS

Quinazoline compounds are potent inhibitors of kinetoplastid parasites

Perfluorinated building blocks can be exploited to rapidly generate a broad range of polyfluorinated drug-like molecules. Previous studies from our group used this strategy to generate a series of 2,6-disubstituted-4,5,7-trifluorobenzothiophenes that demonstrated promising activity against *T. cruzi*, as well as the related kinetoplastid parasites *T. brucei* spp., causative agents of human and animal African trypanosomiasis, and *Leishmania donovani*, responsible for visceral leishmaniasis (18). In the course of these studies, it became evident that this fused 6,5 heterocyclic core skewed activity specifically towards *T. brucei* spp., rather than *T. cruzi* and *L. donovani*. Given that the initial goal of our current study was to develop compounds with broad spectrum anti-kinetoplastid activity, we employed a scaffold hopping approach to design fused heterocyclic compounds with the trifluorinated core maintained that proved essential for all phenotypic activity. Ultimately, reactions of pentafluorophenylacetonitrile with ring-forming reagents, including amidines, were performed to yield new drug-like trifluorinated quinazolines (**Fig. 1A**).

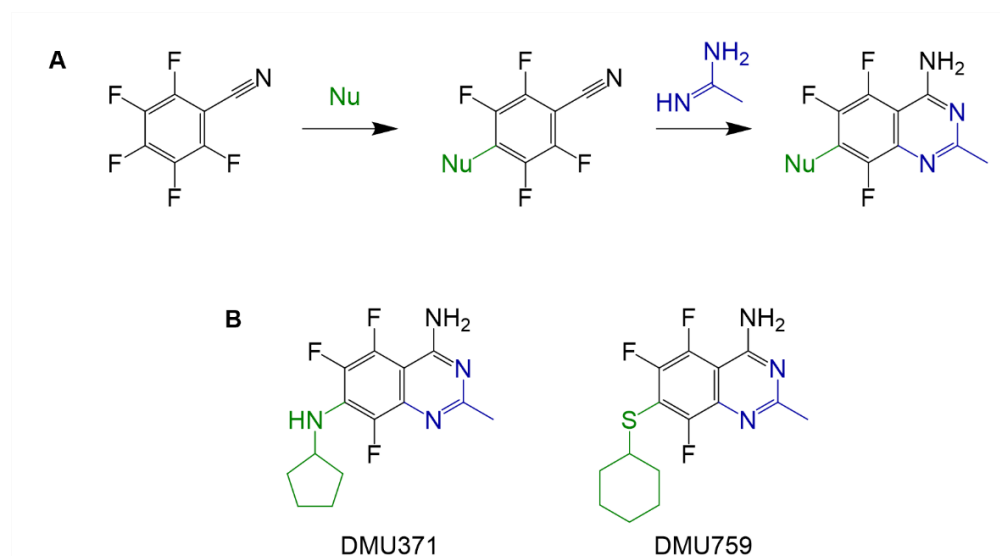


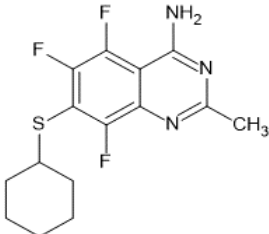
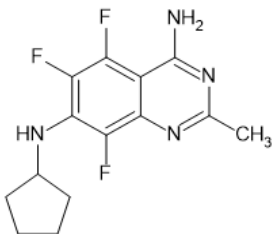
Fig. 1. Generation of trifluorinated quinazolines. (A) Schematic shows the synthesis strategy for generating trifluorinated quinazolines. (B) Shown are the two lead compounds, DMU371 and DMU759, that were further characterized and their mechanism of action investigated. Nu denotes nucleophilic addition.

Early compounds developed within this series demonstrated *in vitro* potency against a range of kinetoplastid parasites indicating the broad utility of the fluorinated quinazoline scaffold. A combinatorial chemistry approach was used to further explore the impact of modifications at positions 2, 4 and 7 of this scaffold. Mouse liver microsome assays revealed that compounds within this series with demonstrated potent anti-kinetoplastid activity ($EC_{50} < 1 \mu M$) were prone to high rates of intrinsic clearance indicative of metabolic instability. However, this liability was not linked to the quinazoline core itself. Therefore, two lead compounds, DMU371 and DMU759 (**Fig. 1B**) were selected for further study. These two compounds demonstrated efficient anti-kinetoplastid activity (**Table 1** and **table S1**) and acceptable ADME profiles (excluding metabolic stability)

(table S2). Thus, DMU371 and DMU759 were selected for subsequent target deconvolution and validation studies.

Understanding the mechanism of action and molecular targets of compounds identified through phenotypic screening can greatly facilitate the drug discovery process. Once the molecular target is known, target-focused and structure-guided strategies to improve compound potency, selectivity and pharmacokinetic properties, such as metabolic stability, can be developed. Knowing the target of a phenotypically active compound can be vital in efficiently ceasing development of compounds acting through an undesirable mechanism of action. This is particularly relevant to drug discovery for Chagas disease where a considerable proportion of hits identified through phenotypic screening have been found to target CYP51 (15), a discredited target following the failure of posaconazole in clinical trials (11). With this in mind, our primary goal was to determine the molecular targets of this quinazoline series to support further development.

138 **Table 1. DMU759 and DMU371 EC₅₀ values in wildtype and transgenic *T. cruzi* strains and human cell lines**

Organism	Cell line	Parasite stage	DMU759		DMU371	
				Fold-shift (relative to WT)		Fold-shift (relative to WT)
<i>T. cruzi</i> (Sylvio X10/7A1 strain)	WT	Epimastigote	14 ± 0.3	-	63 ± 2.4	-
	KRS1 ^{OE}		134 ± 3	10	624 ± 14	10
	KRS1 ^{S319L}		565 ± 41	41	326 ± 26	5
	WT	Intracellular amastigote (in Vero cells)	16 ± 1	-	205 ± 24	-
	KRS1 ^{OE}		121 ± 19	8	888 ± 117	4
	KRS1 ^{S319L}		1540 ± 130	97	589 ± 57	3
<i>T. cruzi</i> (Tulahuen strain)	WT	Intracellular amastigote (in L6 cells)	18 ± 7		233 ± 86	
Human	HepG2		16900 ± 5380		5820 ± 500	

139 EC₅₀ values represent the weighted mean ± standard deviation of ≥2 biological replicates with each biological replicate comprised of ≥2

140 technical replicates. For *T. cruzi* (Tulahuen strain), EC₅₀ values represent the mean +/- standard deviation of 4 biological replicates.

Screening of quinazolines against a genome-wide overexpression library

Taking advantage of the fact that our quinazoline series of compounds demonstrated potent activity against all three kinetoplastid parasites (**Table 1** and **table S1**), we screened DMU371 against our genome-wide overexpression library in *T. brucei* (19). The principle underpinning this gain-of-function screen was that overexpression of a drug target would confer resistance to the corresponding drug by increasing the pool of functional protein or by reducing free drug through binding. The bloodstream form of *T. brucei* was transfected with a pooled population of plasmids containing genomic DNA fragments between 3 and 10 kb in size. The final transfected library provided 10-fold genome coverage with >95% of *T. brucei* genes represented. DMU371 was screened against the library at 1.2 μ M, equivalent to twice the established EC₅₀ value of the compound against bloodstream trypanosomes (**table S1**). Growth of the library under selection with DMU371 was suppressed relative to the unselected library during the first 5 days of selection, however, it recovered strongly prior to harvesting on day 8 (**Fig. 2A**). Following compound selection, plasmids maintained by the “resistant” parasite population were harvested and analysed by next-generation sequencing. Mapping of enriched inserts to the *T. brucei* 927 strain assembled genome revealed that 97% of all mapped reads (4.4 million) aligned to a single region of chromosome 8. This genomic fragment encompassed the entire open reading frame encoding lysyl tRNA synthetase 1 (*KRS1*, Tb927.8.1600), as well as part of the neighboring gene encoding a putative ubiquitin protein ligase (Tb927.8.1590) (**Fig. 2B**, **table S3**). As the only intact gene encoded by this enriched genomic fragment, we hypothesized that overexpression of KRS1 likely conferred resistance to DMU371 thus identifying this enzyme as a putative molecular target of this quinazoline.

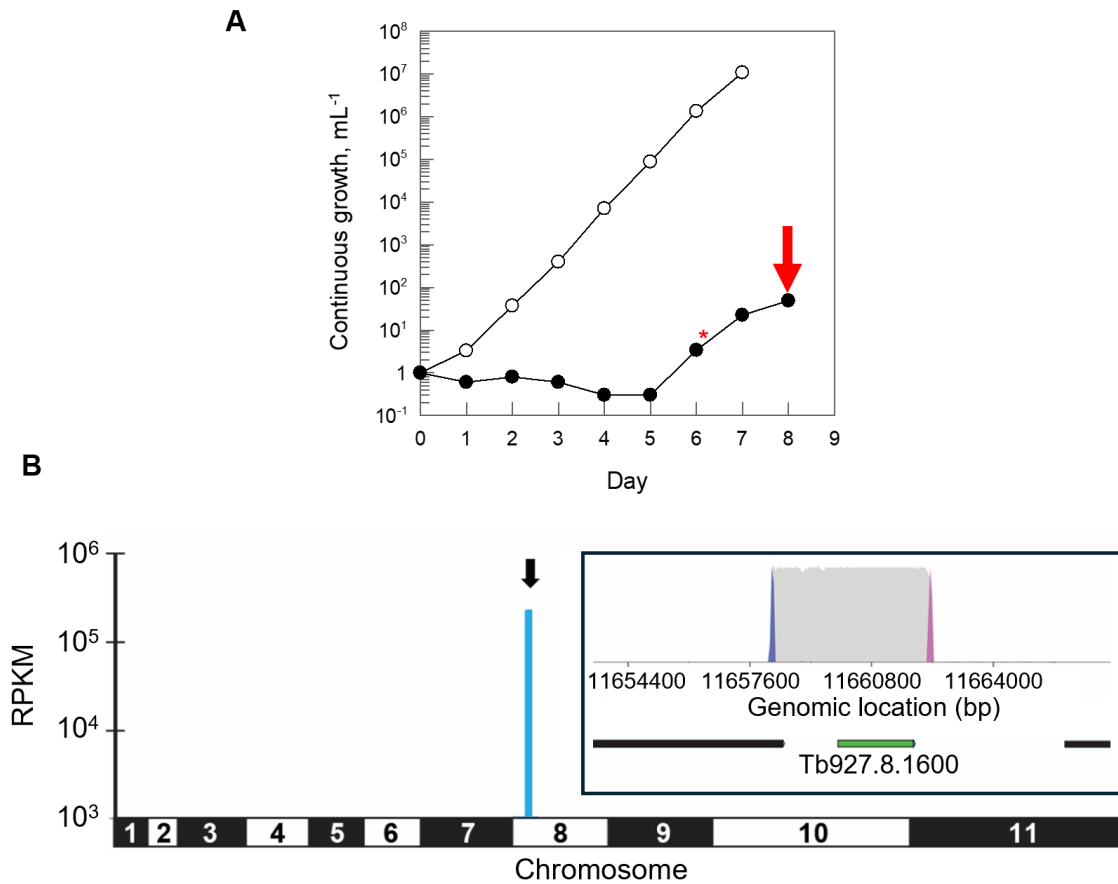


Fig. 2. Genome-wide overexpression library screen with DMU371. The library comprises a pooled population of bloodstream form *T. brucei* transfected with overexpression plasmids containing genomic DNA fragments between 3 and 10 kb in size. The final transfected library provides 10-fold genome coverage with >95% of *T. brucei* genes represented. The parasite library is grown in the presence of test drug and genomic DNA is harvested from those able to survive selection. Next generation sequencing identifies the genomic fragments harbored by “drug resistant” parasites revealing overexpressed proteins and potential drug targets (19). (A) Growth of the genome-wide overexpression library in the presence or absence of DMU371 selection at a concentration equivalent to twice the established EC_{50} value. Asterisk indicates sub-culturing of the culture and addition of fresh compound. The arrow indicates when the library was harvested

for genomic DNA preparation. (B) Shown is the genomewide map resulting from the overexpression library screen with DMU371. RPKM, reads per kilobase of transcript per million mapped reads. Inset shows the top fragment hit of this library screen containing the full coding sequence of lysyl-tRNA synthetase (Tb927.8.1600). Gene of interest is highlighted in green, other protein-coding regions are indicated in black. Blue and pink peaks represent forward and reverse barcodes (in the sense orientation), respectively. Grey peaks are all other reads (table S3).

Genetic validation of KRS1 as the target of DMU371 and DMU759

Aminoacyl-tRNA synthetases (aaRS), ubiquitous enzymes that are essential for protein translation, are considered attractive therapeutic targets in a number of infectious diseases, including malaria, tuberculosis and cryptosporidiosis (20-23). These enzymes catalyze aminoacylation of transfer RNA (tRNA) with their appropriate amino acids. This process, often referred to as tRNA-charging, occurs in two distinct reaction steps: amino acid activation where the amino acids are activated by ATP to yield AMP-activated amino acids followed by tRNA acylation where cognate amino acids are transferred onto tRNAs (Fig. S1). Subtle structural differences in the active sites of a variety of pathogen versus human aaRS have been successfully exploited to design potent and selective inhibitors of these enzymes (21, 22). *T. brucei*, and kinetoplastids more broadly, maintain two copies of *KRS*, both encoded by the nuclear genome. *TbKRS2* more closely aligns to the equivalent aaRS in bacteria, maintaining a C-terminal extension responsible for targeting the protein to the mitochondria where it is cleaved to produce a mature, functional protein (Fig. S2) (24). *TbKRS1*, the putative target of DMU371, is more similar to aaRS from apicomplexan parasites and localizes to the cytoplasm. Across the three major kinetoplastid pathogens, the similarity between *KRS1* and *KRS2* ranges from 30 to 40% (Fig. S2).

The results of our overexpression library screen suggested that DMU371 was a specific inhibitor of *T. brucei* KRS1. To validate this hypothesis, we next generated a clonal *T. brucei* cell line specifically overexpressing *TbKRS1* (*TbKRS1*^{OE}). Elevated expression of *TbKRS1* in these transgenic parasites, relative to wildtype parasites, was confirmed by label-free mass spectrometry quantification (**Fig. S3A**). Compared to wildtype *T. brucei* parasites, *TbKRS1*^{OE} parasites demonstrated ~5-fold reduction in susceptibility to the established selective KRS1 inhibitor DDD01510706 (20, 25), indicating that overexpression of *TbKRS1* was able to functionally complement the compound-inhibited enzyme (**table S4**). In keeping with our library screen, overexpression of *TbKRS1* in bloodstream trypanosomes conferred a similar 7-fold resistance to the representative quinazoline DMU371 (**table S1**) as well as 9-fold resistance to DMU759. These data supported our hypothesis that KRS1 was the molecular target of DMU371 in *T. brucei* and indicated that compounds within our quinazoline series likely shared the same mechanism of action.

Given that DMU371 and DMU759 were pan-active against all kinetoplastid parasites screened to date (**Table 1, table S1**), we next sought to determine whether overexpression of KRS1 homologs in *L. donovani* and *T. cruzi* would also confer resistance to both compounds. Transgenic cell lines overexpressing *L. donovani* and *T. cruzi* KRS1 enzymes were generated, with successful overexpression again confirmed by label-free mass spectrometry quantification (**Fig. S3**). *L. donovani* promastigotes overexpressing *LdKRS1* were 13-fold and 4-fold less susceptible to DMU759 and DMU371, respectively (**table S1**). Similarly, *T. cruzi* epimastigotes overexpressing *TcKRS1* (*TcKRS1*^{OE}) demonstrated 10-fold resistance to these compounds compared to wildtype *T. cruzi* epimastigotes (**Table 1**). Importantly, when grown as intracellular amastigotes within Vero cells, the medically relevant mammalian infective stage of the parasite, *TcKRS1*^{OE} retained

resistance to both compounds (**Table 1**). Collectively, these data supported KRS1 as the common molecular target of these quinazolines in all three major kinetoplastid pathogens.

Quinazolines DMU371 and DMU759 bind to the ATP-binding pocket of KRS1

Previous studies have confirmed that DDD01510706, a chromone inhibitor of *P. falciparum* and *Cryptosporidium parvum*, binds to the ATP-binding pocket of KRS1 in both parasites (21, 25). Mutation of a serine residue (S344) to a leucine residue within the ATP-binding pocket of the *P. falciparum* KRS1 conferred resistance to DDD01510706, with the bulkier leucine residue preventing binding of the inhibitor. Notably, the serine residue is conserved in all three kinetoplastid KRS1 enzymes.

To investigate the possibility that DMU371 and DMU759 exploited the same ATP-binding pocket as DDD01510706, *T. brucei*, *T. cruzi* and *L. donovani* cell lines bearing a serine-to-leucine mutation in the residue equivalent to *PfKRS*^{S344} were generated, either through oligonucleotide targeting (*Tc*, *Tb*) (26) or CRISPR-Cas9 gene editing (*Ld*) (27). All three mutated cell lines (*LdKRS1*^{S324L}, *TcKRS1*^{S319L} and *TbKRS1*^{S323L}) demonstrated reduced susceptibility to both quinazolines (**Table 1, table S1**) indicating that both compounds likely occupied the ATP-binding pocket of the KRS1 enzyme. Interestingly, these point mutations conferred marked resistance to DMU759 in *L. donovani* (12-fold), *T. cruzi* (41-fold) and *T. brucei* (58-fold), relative to susceptibility of wildtype parasites (**Table 1, table S1**). Similar resistance was observed when the cell lines were screened with DDD01510706 (**table S4**). However, these transgenic parasite lines were only moderately resistant (between 3-fold and 5-fold) to DMU371 perhaps suggesting that this compound exploited a slightly different binding position compared to DMU759 and DDD01510706. Our data suggested that both quinazolines targeted the ATP-binding pocket of

KRS1 in all three kinetoplastid parasites. We next focused on characterizing these inhibitors further against *T. cruzi*.

Direct evidence of on-target engagement

The gold-standard in target deconvolution studies is to provide evidence of the compound or drug of interest directly binding to its molecular target. This can be achieved in a variety of ways (reviewed in (28)). Here, we aimed to provide unbiased confirmation of DMU371 and DMU759 binding to their molecular target (KRS1) in *T. cruzi* using isothermal proteome profiling (iTPP) (25), a rationalised version of our standard thermal proteome profiling assay (TPP) (29). Both versions of TPP are based on the principle that binding of a drug to its protein target can alter the thermal stability of that target. In the iTPP assay, the relative abundance of proteins in cell lysates is monitored at a single temperature in the presence and absence of test compounds. Increased abundance of a specific protein in the presence of a compound is indicative of thermo-stabilisation of the target as a result of a direct interaction with the ligand.

In the current study, whole cell lysates of *T. cruzi* epimastigotes were prepared and exposed to DMU371 or DMU759 at 10 times their respective EC₅₀ values or DMSO as a vehicle control for 30 minutes. Our previous studies illustrated that the *T. cruzi* epimastigote proteome has a T_m (temperature at which 50% of all proteins are denatured) of ~46°C (29). To maximise the chances of identifying proteins stabilized in the presence of compound, treated and control lysates were incubated at 48°C. Following incubation, insoluble (denatured) proteins were removed, and the abundance of remaining soluble proteins in each treated and control sample was determined by quantitative mass spectrometry. Proteins demonstrating a >1.5-fold shift in abundance (increase or decrease) in the presence of drug were considered as “hits” and putative targets of the

compound. *TcKRS1* was identified as the top hit and most compelling candidate target of DMU371 and DMU759, with the relative abundance of this enzyme increasing considerably in the presence of both compounds and across two biological replicates (**Fig. 3; tables S5, S6**). In addition to *TcKRS1*, two proteins were modestly but consistently stabilized in the presence of DMU371 (**table S5**), whereas five proteins were identified as hits destabilized in the presence of DMU759 (**table S6**). These data provided further evidence that *TcKRS1* was the primary target of these quinazoline compounds.

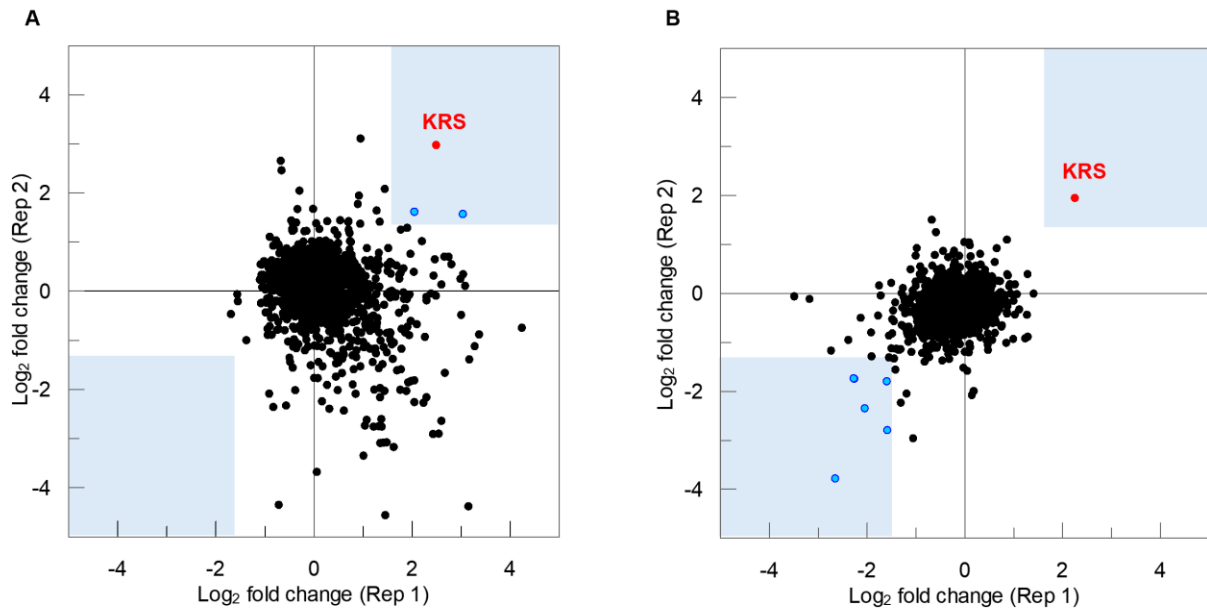


Fig. 3. Isothermal TPP for proteome scale identification of quinazoline targets. Isothermal TPP plots show \log_2 fold change in abundance between compound-treated and untreated *T. cruzi* epimastigote lysates subjected to thermal shock at 48°C across two biological replicates. All proteins identified with >2 unique peptides are shown. “Hits” demonstrating a >1.5-fold shift in abundance (increase or decrease) are shown in blue. *TcKRS1* is indicated in red. Hits for experiments with DMU371 and DMU759 are noted in **tables S5 and S6**, respectively.

Inhibition of *Tc*KRS1 enzyme activity

KRS1-mediated synthesis of lysyl tRNA occurs in two distinct steps. In the first step, lysine and ATP are combined to form a lysyl-5'-AMP intermediate with the concomitant release of pyrophosphate. In the second step of the reaction, the lysyl-5'-AMP intermediate is conjugated to the 3' of the cognate tRNA. To confirm that binding of our quinazoline compounds inhibited enzyme activity, *Tc*KRS1 was recombinantly expressed and purified. The enzymatic activity of the recombinant protein was monitored based on a previously reported biochemical assay (25). The assay monitors the first step of the aminoacylation reaction and specifically the production of pyrophosphate that is converted to free phosphate by a coupled enzyme (pyrophosphatase), the free phosphate is then quantified by the addition of the reagent BIOMOL Green (**Fig. S1**). As expected, both DMU371 and DMU759 proved to be potent inhibitors of *Tc*KRS1 activity in this assay with mean IC₅₀ values of 185 nM (95% confidence interval, 98–352 nM, *n*=7) and 15 nM (95% confidence interval, 5–43 nM, *n*=4), respectively. Importantly, in parallel assays, these quinazolines were not potent inhibitors of the human ortholog of KRS1, with mean IC₅₀ values of 7170 nM (95% confidence interval, 2860–18010 nM; *n*=4) and 9800 nM (95% confidence interval, 5240–18300 nM; *n*=4) for DMU759 and DMU371, respectively (**Table 2**). In addition, only partial inhibition of the human KRS1 enzyme was observed, in contrast to *Tc*KRS1, where full inhibition of the enzyme was measured. These IC₅₀ values were consistent with the degree of selective toxicity demonstrated by both compounds against *T. cruzi* parasites (epimastigotes and intracellular amastigotes) relative to a human HepG2 cell line (**Table 1**).

Table 2. Activity of quinazoline compounds in TcKRS1 and human KRS enzyme assays

Enzyme	IC ₅₀ values*, nM (95% CI)	
	DMU759	DMU371
TcKRS	15 (5 - 43)	185 (98 - 352)
human KRS	7170 (2860 - 18010)	9800 (5240 – 18340)

*IC₅₀ values represent the mean with 95% confidence intervals determined from at least four biological replicates ($n \geq 4$). The 95% confidence interval indicates the concentration range within which IC₅₀ values are likely to fall.

Crystal structures reveal key inhibitor binding interactions in the KRS ATP-binding pocket

To gain insight into the molecular interactions that these inhibitors made within the ATP-binding pocket of KRS1, we aimed to generate a high-resolution crystal structure with ligand bound. In the first instance, we attempted to crystallize recombinant TcKRS1 in the presence of either DMU371 or DMU759. However, despite multiple attempts in a wide range of crystallization conditions, high quality crystals could not be generated. Previous studies have demonstrated the propensity of KRS1 from *C. parvum* (CpKRS1) to crystallize, producing crystals that diffract to high-resolution (21). Given that the ATP-binding pockets of the KRS1 enzymes of *T. cruzi* and *C. parvum* only differ by four amino acids, we synthesized a *T. cruzi*/*C. parvum* hybrid enzyme (TcCpKRS1) by mutating the four variable amino acids in the CpKRS1 enzyme to the corresponding *T. cruzi* residues (I290L, A309S, M310V and I538L) (**Fig. S4**). This hybrid enzyme readily crystallized in the presence of lysine, with the resulting crystals then soaked in the presence

of DMU371 or DMU759. *TcCpKRS* crystals soaked with DMU759 did not produce a liganded structure, however, those soaked with DMU371 diffracted to 1.6Å revealing *TcCpKRS* bound to inhibitor (**table S7, Fig. 4A**). DMU371 was bound within the ATP-binding pocket of the enzyme, with the quinazoline ring of the inhibitor in space usually occupied by the adenine ring of ATP, forming π - π stacking interactions with F307 (equivalent to F317 in *TcKRS1*) and R523 (equivalent to R536 in *TcKRS1*) (**Fig. S5**). The cyclopentyl moiety of DMU371 occupies a position similar to that adopted by the furan ring of ATP, in a pocket created by the lysine substrate S309 (equivalent to S319 in *TcKRS1*) and surrounding amino acids and lined by three water molecules (**Fig. 4A, B**). We hypothesized that DMU759 occupied a similar binding position to DMU371. Given that this analog was slightly larger than DMU371, due to its cyclohexyl ring and bridging sulfur group, binding may have required a modest conformational change within the active site of KRS1 that was not possible in the rigid crystallized state. However, this modest change may have led to improved Van der Waals interactions between the inhibitor, lysine substrate and enzyme, explaining the superior potency of the DMU759 compound relative to DMU371 (**Table 1**). Based on our *TcCpKRS1* liganded structure, mutation of S309 to leucine is likely to hinder the binding of DMU371 in a relatively minor way (**Fig. 4C**). In contrast, this mutation would likely cause a greater clash with the larger cyclohexyl group of DMU759, explaining the enhanced resistance seen with this analog compared to DMU371 (**Table 1**).

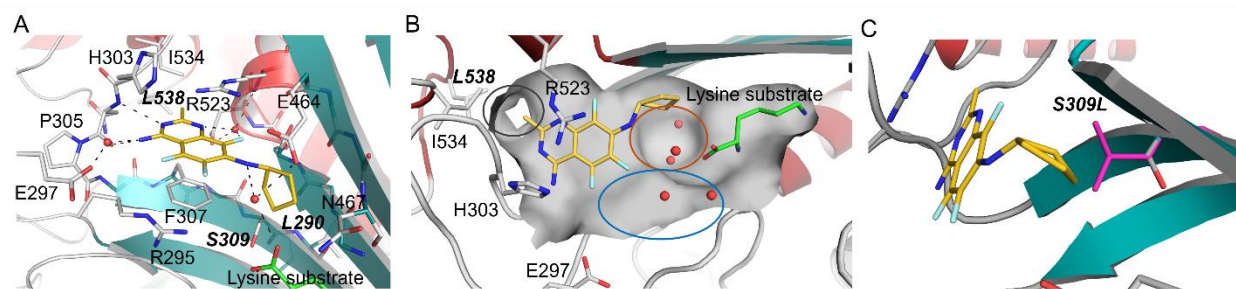


Fig. 4. Crystal structure of TcCpKRS1 with DMU371 bound to the active site. (A) Shown is the crystal structure of TcCpKRS1 with DMU371 (yellow) bound to the active site in the presence of lysine substrate (green). Water molecules are indicated in red and hydrogen bonding interactions formed with water molecules are represented as black dashed lines. Key residues are labeled using CpKRS1 numbering. *C. parvum* residues mutated to their *T. cruzi* counterparts are shown in bold italics. (B) Three unoccupied regions of the active site that could be exploited for future quinazoline analog development are highlighted with red, blue and dark grey ovals. The surface of the enzyme is shown in grey and water molecules are shown in red. (C) The most likely conformation of S309L is shown in magenta. Proximity to the cyclopentyl moiety of DMU371 (yellow) and potential for steric clash is evident.

***In vivo* efficacy of DMU759 in a mouse model of acute *T. cruzi* infection**

Bioluminescent mouse models of infection have revolutionized our understanding of *T. cruzi* biology and Chagas disease pathogenesis (30, 31). We now recognize the dynamic nature of chronic infection with *T. cruzi*, the importance of the gut as a permissive niche for parasites, and the requirement to kill persister non-replicating parasite stages to achieve cure. In acknowledgment of the sub-optimal metabolic stability of both quinazoline compounds (Table S2), we opted to assess our most potent *in vitro* compound DMU759 in an acute rather than a chronic mouse model

of *T. cruzi* infection. These initial studies were aimed at providing proof-of-concept that inhibitors of TcKRS1 could reduce parasitemia *in vivo*.

To assess the *in vivo* efficacy of DMU759, BALB/c mice were acutely infected with *T. cruzi* CL Brener strain (10 days post-infection) and were treated orally for 5 consecutive days with 50 mg/kg DMU759 *BID* (*n*=3) and 100 mg/kg benznidazole *QD* (*n*=3) as a positive control (32). Parasite burden was monitored in treated and control mice via bioluminescence imaging. In mice treated with the standard of care treatment benznidazole, parasite burden was reduced close to the limit of detection, whereas treatment with DMU759 reduced parasite burden up to 81% (**Fig. 5**). Retrospective analysis of DMU759 concentration in blood following oral dosing of mice revealed that total blood concentrations comfortably exceeded EC₉₉ (concentrations required to kill 99% of parasites) for up to 4 hours post dosing (**Fig. S6**). However, once these concentrations were corrected to account for DMU759 bound to plasma proteins (89% bound), it was confirmed that the free blood concentration of this compound did not exceed the established EC₉₉ and only surpassed the EC₉₀ for ~2 hours. In keeping with our earlier mouse liver microsome data (**Table S2**), DMU759 was also subject to rapid metabolism and blood concentrations rapidly declined after peaking one hour post dosing. Bearing in mind the pharmacokinetic limitations of DMU759 with regard to plasma protein binding and metabolic instability, the efficacy achieved with this compound *in vivo* suggests that pharmacokinetically optimized analogs from this series or others targeting KRS1 may have potential for effectively treating *T. cruzi* infection in this acute mouse model of Chagas disease.

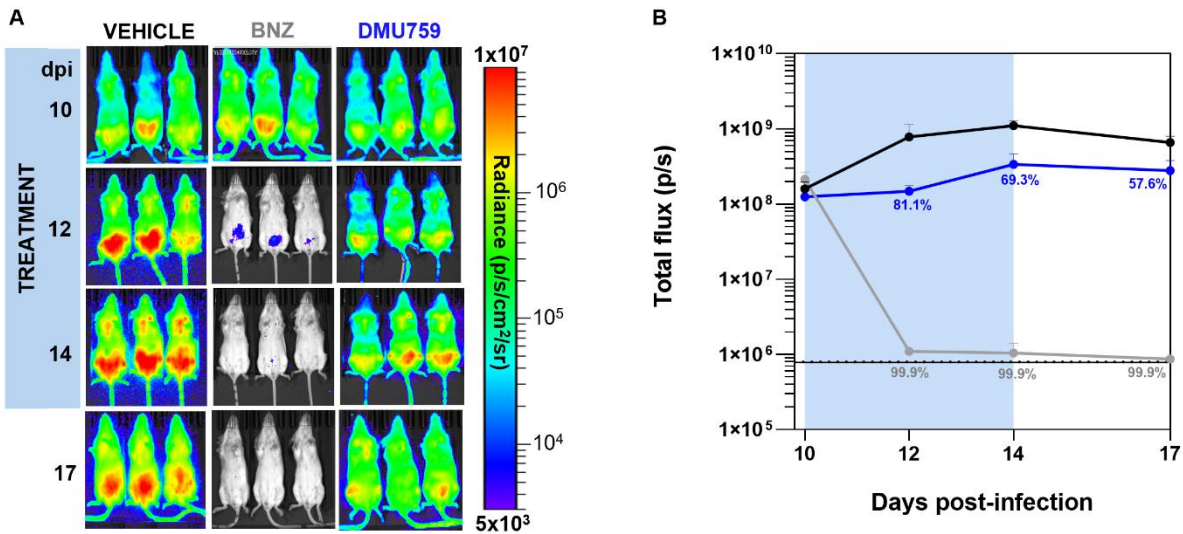


Fig. 5. Assessment of DMU759 efficacy in a murine model of acute Chagas disease. (A) BALB/c mice infected with bioluminescent *T. cruzi* CL-Brener strain were treated for 10 days post-infection (dpi) for 5 days by oral gavage with 100 mg/kg benznidazole (BNZ) ($n=3$) once daily, or with DMU759 50 mg/kg ($n=3$) twice daily. Ventral images of each mouse are shown at various timepoints following infection. Heat maps are shown on a \log_{10} scale and indicate bioluminescence intensity related to parasite burden (blue, low intensity; red, high intensity). The minimum and maximum radiances for the pseudocolor scale are shown. **(B)** Graph presents the mean bioluminescence (photons per second, p/s) determined by in vivo imaging of treated and untreated mice infected with *T. cruzi*. Treatment groups and dosing regimens are indicated. The black horizontal unbroken line indicates background bioluminescence total flux established from uninfected mice ($n=3$), with the dashed line indicating SD above the average.

DISCUSSION

In our current study, we used unbiased approaches to identify the molecular target of a new quinazoline series demonstrating promising phenotypic activity against a range of kinetoplastid parasites including *T. cruzi*, *T. brucei* and *L. donovani*. We identified the amino acyl tRNA synthetase KRS1 as the molecular target of these compounds. Focused studies in *T. cruzi* revealed that compounds from this series bound specifically within the ATP-binding pocket of KRS1. Of particular importance, *in vivo* studies in a murine model of acute Chagas disease provided proof-of-concept of the therapeutic potential of KRS1 inhibitors for treating *T. cruzi* infection. This efficacy was achieved despite sub-optimal metabolic stability of the test compound, DMU759. Future studies will focus on further developing the series to increase metabolic stability whilst retaining potency facilitated by our high-resolution liganded structure. This structure revealed a number of pockets close to the current inhibitor binding site (see **Fig. 4B**) that could be exploited to improve ligand binding. Metabolite identification studies will be vital to pinpoint the metabolic liabilities of this quinazoline series, however, we will also use two general strategies to improve stability namely to reduce LogD of the series and to look for the potential to achieve a scaffold hop. For instance, changing the cyclo-hexyl/pentyl ring would be a rapid route to reducing hydrophobicity within the series and changes at the 7-position of the quinazoline core have been shown to modulate phenotypic activity. H-bond interactions formed by the amino-quinazoline are well characterized thanks to our protein-ligand structure confirming the pyrimidine ring portion of this series will be difficult to replace, but this can be balanced by exploration of other 6,6 ring systems.

The fact that mutation of a single amino acid in the KRS1 active site could confer >20-fold resistance to the two lead compounds, DMU371 and DMU759, *in vitro* raises the possibility that

this quinazoline series, or the target itself, may be associated with high drug resistance potential in the clinic. We have not yet assessed the relative fitness of parasites bearing KRS1 mutations *in vivo* and so cannot make any predictions regarding the likelihood of their transmission. Furthermore, the overwhelming majority of Chagas disease infections are zoonotic, with the animal reservoirs not previously having been exposed to drug treatment. This, together with the fact that parasite burden in patients with Chagas disease is low, greatly reduces the chances of acquired drug resistance emerging to any anti-chagasic treatment. However, the existence of naturally occurring resistance cannot be discounted. As required for any new chemical entity, our lead and candidate compounds will be screened to ensure they retain potency against clinical isolate panels. In addition, we will carefully monitor clinical isolate sequencing data to determine the frequency of mutations of concern within KRS1. Finally, we will look for appropriate partner compounds for our KRS1 inhibitors with a view to developing a combination therapy to further mitigate resistance risk.

Our understanding of the dynamics of *T. cruzi* infections has evolved considerably over the last decade. We have come to recognize the importance of persister forms of the parasite that are often less susceptible to drug treatment. We also recognize the requirement for drugs to kill all parasite forms to deliver sterile cure. *T. cruzi* persisters are considered transiently quiescent, however, we do not know the true metabolic status of these parasites. One could argue that as protein synthesis is likely downgraded in persisters that drugs targeting enzymes involved in protein synthesis, such as KRS1, may be less effective against slow growing or static forms of the parasite. The counter argument is that persister parasites will likely require some level of protein synthesis, particularly as they exit quiescence, thus KRS enzymes are viable drug targets. Notably, in other organisms, amino acyl tRNA synthetases can perform a broad range of essential, non-

canonical functions beyond covalent binding of an amino acid to a corresponding tRNA (33, 34). Further work will be required to determine all of the functions performed by KRS1 in *T. cruzi* and to determine whether these functions are required for survival of persister forms of this parasite.

Our study has limitations. The current Target Product Profile guiding the development of anti-chagasic drugs stipulates that all future chemotherapies must be capable of treating both chronic and acute stages of the disease (35). To date, we have not been able to demonstrate that the quinazolines described in this study, or *TcKRS1* inhibitors in general, are capable of fulfilling these criteria. Having developed quinazolines with improved metabolic stability and reduced plasma protein binding, our goal will be to assess these compounds in chronic models of infection and in washout assays *in vitro* that will be used to examine the ability of compounds to deliver sterile cure *in vitro* (15, 36) and accurately predict efficacy *in vivo*.

In conclusion, our studies identified a promising chemical quinazoline series demonstrating partial efficacy in a murine model of acute Chagas disease. We chemically validated KRS1 as a promising drug target in *T. cruzi*. We hope that this research can be leveraged in the future to deliver much needed treatment options for this devastating infectious disease.

MATERIALS AND METHODS

Study design

The objective of this study was to identify the molecular target of previously identified quinazoline compounds demonstrating promising *in vitro* activity against *T. cruzi* and related trypanosomatids. Our study aimed to provide target-based information that could be used to guide the development of quinazolines with improved pharmacokinetic properties while retaining potency. Multiple approaches were used to identify and validate the molecular target of two representative compounds from this series, DMU371 and DMU759. Approaches utilized included screening against our *T. brucei* genome-wide overexpression library, drug sensitivity assays against panels of transgenic parasite cell lines, isothermal protein profiling and recombinant *TcKRS1* inhibition assays. All biological assays were carried out in technical and biological replicate (≥ 2). Quantitative proteomics studies were carried out in technical replicate. Crystallographic studies were carried out to determine the binding orientation of our compounds in the active site of KRS1. Finally, the therapeutic potential of quinazolines targeting *TcKRS1* was assessed in a murine model of acute Chagas disease. Three mice, not predetermined using statistical methods, were randomly selected for inclusion in the study. A small cohort was used based on the high reproducibility of the bioluminescence mouse model and to adhere to animal welfare considerations. Investigators were not blinded to group allocation during experimental procedures or data analysis. Imaging data were collected as both optical images and quantitative bioluminescence, measured as total flux (photons/second), calculated from the sum of ventral and dorsal images. Quantification was performed manually by drawing individual regions of interest

(ROIs) for each mouse, including naïve animals, to reduce potential selection bias and to increase the precision of area selection.

Animal work was performed under UK Home Office project license P9AEE04E4 and approved by the LSHTM Animal Welfare and Ethical Review Board. Procedures were performed in accordance with the UK Animals Scientific Procedures Act (1986).

Cell lines and culture conditions

T. cruzi epimastigotes of the Silvio strain (MHOM/BR/78/Silvio; clone X10/7A) were maintained at 28°C in RPMI 1640 medium (Merck) supplemented with trypticase peptone (4.9 mg/ml), HEPES (20 mM), haemin (20 µg/ml), and foetal bovine serum (FBS, 10%), as previously described (29). *T. cruzi* metacyclic trypomastigotes were obtained and maintained, as previously described (29). Briefly, late-log epimastigotes were seeded at 10⁶ cells/ml in RTH/FBS and differentiated into trypomastigotes after 7 days at 28°C. Vero cells were infected with trypomastigotes for 12 hours in Dulbecco modified Eagle medium (DMEM) supplemented with 5% FBS, at 37°C in the presence of 5% CO₂. Infected Vero cells were washed 3× with DMEM/FBS to remove extracellular parasites, and medium was replaced every two days until trypomastigotes re-emerged. Three rounds of infection were performed before trypomastigotes were harvested for drug sensitivity assays. For drug sensitivity assays carried out at the Swiss Tropical Institute, a *T. cruzi* cell line (Tulahuen C2C4) expressing the β-galactosidase gene *LacZ* was propagated in L6 rat skeletal myoblasts (ATCC CRL-1458) as previously described (37).

T. brucei bloodstream forms S427 (T7RPOL TETR NEO) and 2T1 were maintained at 37°C in HMI-11 medium (38) in the presence of 5% CO₂. *T. b. rhodesiense* STIB 900 strain was maintained in HMI-9 medium supplemented with 15% heat-inactivated horse serum.

L. donovani (LdBOB) promastigotes derived from MHOM/SD/62/1S-CL2D were maintained at 28°C in modified M199 medium, as previously described (39).

Human HepG2 cells (ECACC 85011430) were cultivated at 37°C in minimal essential medium (MEM) supplemented with GlutaMax (1×, Thermo Fisher), 10% (v/v) fetal bovine serum (FBS), MEM non-essential amino acids (1×, Sigma) and in the presence of 5% CO₂, as previously described (29). Cells were passaged twice weekly through detachment of adherent cells with trypsin/EDTA (Sigma) and subsequent dilution into fresh medium.

Vero cells (African green monkey kidney epithelial cells, ECCAC 84113001) were maintained at 37°C, in 5% CO₂, in DMEM supplemented with 10% FBS, as previously described (40). Cells were passaged twice weekly.

Drug sensitivity assays

The relative potency of test compounds against *T. cruzi* epimastigotes (29), *T. b. brucei* bloodstream forms (41), *T. b. rhodesiense* bloodstream forms (42), *L. donovani* promastigotes (43) and Hep G2 cells (29) were established as previously described. The potency of test compounds on intracellular *T. cruzi* (Sylvio, X10/7A1) were determined in 96-well plates as previously described (29). Data were fitted to the two-parameter equation below, where y is % cell growth, $[I]$ is the inhibitor concentration and m is the slope, using GraFit (Erithacus Software).

$$y = \frac{100}{1 + \left(\frac{[I]}{EC_{50}}\right)^m}$$

Drug sensitivity assays with *T. cruzi* (Tulahuen)-infected L6 rat skeletal myoblasts were carried out as previously described (37).

Generation of a KRS1 overexpression construct and transgenic cell line

We began by assembling the genome of our in-house clone of *T. cruzi* X10/7, known as X10/7A1, using whole-genome sequencing (WGS) data derived from short reads via the SPAdes software (44). To identify the gene of interest (*TcKRS1*), we performed a homology search within the assembled genome using the CDS of TcSYL_0202360 (clone X10/1) as the query in the MMseqs software (45). Upon locating *TcKRS1*, we extracted a region encompassing 1000 base pairs upstream and downstream of the CDS. This region was used to generate the overexpression construct described below.

The *TcKRS1* CDS was synthesised by GeneArt (Thermo) and cloned into the *T. cruzi* expression vector pTREX (46) via EcoRI and XhoI restriction sites, generating pTREX-*TcKRS1*. The accuracy of cloning was confirmed by Sanger sequencing using primers pTREX-Fw and pTREX-Rv (Table S8). Mid-log *T. cruzi* epimastigotes (2×10^7) were transfected with 10 μ g pTREX-*TcKRS1* using the Human T cell Nucleofector kit (Lonza) and Amaxa Nucleofector program U-033. Transfected cells were selected with G148 (250 μ g/ml), and individual clones were generated by limiting dilution. Elevated *TcKRS1* expression in these transgenic clones, relative to wild type, was confirmed by quantitative proteomics.

The *TbKRS1* (Tb927.8.1600) ORF was synthesised by GeneArt (Invitrogen) and cloned into the tetracycline-inducible expression vector pRPa via HindIII and BamHI restriction sites (47), to generate pRPa-*TbKRS1* with the accuracy of cloning confirmed by Sanger sequencing using primers LBT-074 and LBT-075 (table S8). Mid-log *T. brucei* bloodstream trypanosomes (2×10^7) were transfected with 10 μ g pRPa-*TbKRS1* following digestion with AscI to linearise, using the Human T cell Nucleofector kit (Lonza) and Amaxa Nucleofector program X-001. Transfected parasites were seeded into a 96-well plate at a density of 3.2×10^3 cells/ml under

selection with hygromycin (2.5 µg/ml) and phleomycin (1 µg/ml) and single clones recovered. *TbKRS1* overexpression in harvested clones was evaluated by quantitative proteomics.

LdKRS1 (LdBPK_150270.1) was amplified from *L. donovani* (LdBOB) gDNA by PCR using primers LBT-094 and LBT-095 (**table S8**) and cloned into the pIR1 expression vector via a *Bgl*III restriction site, generating pIR1-*LdKRS1*. The accuracy of cloning was confirmed by Sanger sequencing with the sequencing primers pIR1-SAT-*Bgl*III-SeqF/R (**table S8**). Mid-log *L. donovani* promastigotes (10^7) were transfected with linearised pIR1-*LdKRS1* (10 µg), following digestion of the plasmid with *Swa*I, using the Human T cell Nucleofector kit (Lonza) and Amaxa Nucleofector program V-033. Transfected cells were seeded in a 96-well plate at 100 cells/well under selection with nourseothricin (100 µg/ml) to generate clones. *LdKRS1* overexpression from resulting single cell clones was evaluated by quantitative proteomics.

Generation of cell lines bearing KRS1 mutations

T. cruzi parasites bearing the S319L mutation in KRS1 were generated via CRISPR-free oligo-engineering (26). Wildtype epimastigotes (2×10^7) were transfected with oligo LBT-148 (50 µg), as described above, and the resulting parasites were selected with DMU759 at 10× its established EC₅₀ value. Parasites surviving DMU759 selection were cloned by limiting dilution, and four clones were selected for further evaluation. Genomic DNA was harvested from clones and the region of *TcKRS1* from nucleotide 827-1447 was PCR-amplified from gDNA recovered from the clones with primers LBT-165 and LBT-166. The resulting PCR products were Sanger sequenced using the primer KRS2-qPCR-Rev (**table S8**).

T. brucei KRS1 S323L mutants were also generated using CRISPR-free oligo-engineering. Bloodstream trypanosomes (2×10^7) were transfected, as described previously, with oligo LBT-175

(50 µg). Transfected parasites were then selected with DMU759 at 10× its established EC₅₀ value. The parasites surviving selection with DMU759 were then cloned by limiting dilution and four clones were selected for further evaluation. The *TbKRS1* ORF was amplified by PCR using primers JD081 and JD082 (**table S8**). The resulting PCR products were Sanger-sequenced with primer JD085.

L. donovani KRS1 S324L mutants were generated by CRISPR-Cas9 gene-editing in a WT background constitutively expressing Cas9 and T7 RNA polymerase, as previously described (48). In brief, a sgRNA template directing Cas9 cleavage of the endogenous KRS alleles was generated by PCR-elongation of primer LBT-115 with primer G00, as previously described (27). *L. donovani* promastigotes (2×10^7) were transfected with repair oligo LBT-114 (50 µg). Transfected parasites were selected with DMU759 or DDD01510706 at 10× their respective EC₅₀ values. Surviving parasites were cloned by limiting dilution, and four clones were selected for further evaluation. Genomic DNA was harvested from each clone and *LdKRS1* was PCR-amplified using primers LBT-094 and LBT-095. The resulting PCR products were Sanger-sequenced with primer LBT-085. All primers are shown in **table S8**.

Quantitative proteomics analysis of wildtype and KRS1 overexpressing mutant

The relative protein abundance in the wildtype versus the overexpressing cell line was established as previously described (49), using 3×10^8 parasites per sample. Here, proteins were identified by searching the protein sequence database containing *T. cruzi* Dm28c, *T. b. brucei* TREU927 or *L. donovani* BPK282A1 annotated proteins (downloaded from TriTrypDB 49 <http://www.tritrypdb.org>).

***T. b. brucei* overexpression library screening and data analysis**

DMU371 was screened against a tetracycline-inducible *T. b. brucei* overexpression library. The library was screened, and data processed, as previously described (19). In this instance, the library was selected with DMU371 at 2× its established EC₅₀ value. Associated datasets have been deposited with the National Centre for Biotechnology Information Sequence Read Archive (NCBI SRA) under project code PRJNA1076710.

Isothermal proteome profiling (iTPP)

T. cruzi epimastigote lysates were generated as previously described (29). Isothermal TPP assays were performed as previously described (25). In this instance, lysates were incubated with either DMU371 or DMU759 at concentrations equivalent to 10× their respective EC₅₀ values or in the presence of vehicle (0.1% DMSO, drug-free control) for 30 min at RT and then submitted to a temperature shock for 3 min at 48°C. Data processing and analyses were performed as previously described (25), except proteins were identified via searches against the *T. cruzi* Dm28C proteome (tritypdb.org, version 49).

Cloning, expression and purification of recombinant KRS1

Cloning, expression and purification of recombinant *Hs*KRS has been described previously (21).

For *Tc*KRS1 (TcCLB.508971.30), synthetic DNA codon-optimized for expression in *E. coli* and encoding amino acid residues 54–580 of the *Tc*KRS1 protein was synthesized by Genscript and subcloned into a modified pET15b vector, with an *N*-terminal 6×His tag and a Tobacco Etch Virus (TEV) cleavage site. The resulting plasmid was transformed into *E. coli* BL21(DE3) (Stratagene) for expression. A 10-ml starter culture was grown at 37°C overnight, then used to

inoculate 1 L of LB Autoinduction media that was grown for 48 h at 20°C. Cell pellets were resuspended in buffer containing 25 mM Tris, 500 mM NaCl, 20 mM imidazole, pH 8.5, and lysed using a continuous flow cell disrupter (Constant Systems). Recombinant *TcKRS1* was purified using Ni²⁺ affinity chromatography, the 6×His tag cleaved using TEV protease and the tag and protease removed by a second Ni²⁺ affinity chromatography step. The protein was further purified via size exclusion chromatography, where *TcKRS1* eluted with a mass consistent with the protein forming a dimer. Purified recombinant protein were concentrated to ~1 mg/ml in buffer (25 mM Tris, 150 mM NaCl, 10 % glycerol, pH 7.5) for assay.

Cloning, expression and purification of *TcCpKRS1* was as described for *CpPfKRS1* (25).

***TcKRS1* inhibition assays using BIOMOL Green**

The enzymatic activity of recombinant KRS was determined by monitoring the concentration of pyrophosphate released during the first step of the reaction catalyzed by recombinant *TcKRS1*. The pyrophosphate formed was converted to two inorganic phosphate molecules using a pyrophosphatase enzyme and concentrations of the resulting phosphate were measured using the BIOMOL Green reagent (Enzo Life Sciences). All screening assays were performed in 384-well, clear, flat-bottom plates (Greiner) at room temperature (~23°C) in 50 µl reaction volumes.

To generate IC₅₀ data for test compounds, 10-point inhibitor dose-response curves were prepared in 384-well assay plates using an ECHO 550 acoustic dispenser (Labcyte). Following preparation of the inhibitor curves, assays were carried out for recombinant KRS enzymes as follows: *TcKRS1* assay wells contained r*TcKRS1* assay buffer (100 mM Tris; pH 8, 140 mM NaCl, 30 mM KCl, 40 mM MgCl₂, 0.01% (v/v) Brij and 1 mM DTT) plus 50 nM r*TcKRS1*, 14 µM ATP (~2× *K_m*), 400 µM L-lysine (~2× *K_m*) and 0.5 U/ml pyrophosphatase; *HsKRS* reactions

contained *HsKRS* assay buffer (30 mM Tris; pH 8, 140 mM NaCl, 30 mM KCl, 40 mM MgCl₂, 0.01% (v/v) Brij and 1 mM DTT) plus 200 nM r*HsKRS*, 3.5 μM ATP (~ 2× *K_m*), 6 μM L-lysine (~3× *K_m*) and 0.5 U/ml pyrophosphatase.

All assays were performed by adding 25 μl of assay buffer with enzyme to compound-containing assay wells before the reaction was initiated with the addition of a 25 μl substrate mixture containing L-lysine, ATP and pyrophosphatase. On all assay plates, 0% inhibition (DMSO) and 100% inhibition control wells were included (100% inhibition controls for the *TcKRS1* assay omitted lysine, while reference compound DDD01827593 was used at 100 μM for *HsKRS1* 100% inhibition control wells). Following a 6-h reaction at room temperature, the assays were stopped by the addition of 50 μl BIOMOL Green. The BIOMOL Green signal was allowed to develop for 30 min before the absorbance of each well was read at 650 nm using a PheraStar plate reader (BMG). All liquid-dispensing steps were carried out using a Thermo Scientific WellMate dispenser (Matrix).

ActivityBase (IDBS, version 8.0.5.4) was used for data processing and analysis, with percentage inhibition values determined relative to 0% and 100% inhibition control wells. All IC₅₀ curve fitting was undertaken using ActivityBase XE (version 7.7.1) from IDBS. Percentage inhibition curves for *TcKRS1* and human KRS, were fitted to a four-parameter logistic dose-response equation (XLfit model 203), with pre-fitting for all four parameters, using the equation below, where *A* is no inhibition, *B* is maximum inhibition, *C* is the Log₁₀ (IC₅₀), *D* is the Hill slope and *x* is the inhibitor concentration.

$$y = A + \frac{B - A}{1 + \left(\frac{10^C}{x}\right)^D}$$

Crystallization of the *TcCpKRS1* hybrid enzyme and structure determination

Crystals of *TcCpKRS* were grown in similar conditions to those previously used for crystallization of *CpKRS* protein (21). Protein (30 mg/ml) in storage buffer (25 mM HEPES, 0.5 M NaCl, 5 % w/v glycerol, 2 mM TCEP, pH 7.0), was incubated with 5 mM lysine prior to setting up crystallization drops. Crystals were grown using vapor diffusion in hanging drops, with a reservoir containing 25% PEG 3350, 0.2 M lithium sulphate and 0.1 M Tris, pH 7.8. Crystallization drops consisted of 1 μ l protein solution and 1 μ l of reservoir. For soaking, crystals were transferred into drops consisting of 1 μ l of reservoir and 1 μ l storage buffer containing 10 mM compound. Crystals were harvested after one hour of soaking, cryoprotected using reservoir supplemented with 33% glycerol, and flash frozen in liquid nitrogen.

Data were collected at beamline I04 at Diamond Light Source, at a wavelength of 0.95373 Å. The data were integrated using the DIALS automated pipeline (50) and scaled and merged using Aimless (51). The structure was solved using the structure of *CpKRS* (PDB: 5ELO, (21)) as the search model in Phaser (52). Manual model building was performed using Coot (53) and the structure refined using Refmac (54), incorporated into the CCP4 suite of software (55). The ligand dictionary was prepared using Acedrg (56) and model quality assessed using Molprobit (57). Data collection and refinement statistics are provided in **table S7**.

Murine infections and bioluminescence imaging

Female BALB/c mice (aged 6-7 weeks), purchased from Charles River (UK), were maintained under specific pathogen-free conditions in individually ventilated cages, with a 12 h light/dark cycle. They had access to food and water *ad libitum*. Mice were infected by intraperitoneal injection (i.p) of 1×10^3 bloodstream trypomastigotes derived from CB17 SCID mouse blood [27].

Compounds were prepared in 5% (v/v) dimethyl sulfoxide /95% HPMC suspension vehicle (0.5% (w/v) hydroxypropyl methylcellulose, 0.5% (v/v) benzyl alcohol, 0.4% (v/v) Tween 80 in Milli-Q water). Mice were treated as outlined in **Fig. 5**, with compounds administered by oral gavage. At different days after infection, mice were injected with d-luciferin (150 mg/kg) i.p., anaesthetized using 2.5% (v/v) gaseous isoflurane and imaged using an IVIS Spectrum (Revvity, Hopkinton, MA, USA) 5-10 min later. To estimate parasite burden, mice ventral and dorsal regions of interest were drawn using Living Image 4.7.3 to quantify bioluminescence expressed as total flux (photons/second; p/s). Regions of interest data from infected and not-infected mice were used as controls. Exposure times varied between 30 sec and 5 min, depending on the signal intensity.

Determining DMU759 exposure in mice after oral dosing

DMU759 (50 mg/kg) was orally administered to BALB/c mice. The dose solution was prepared on the day of dosing, and the vehicle was 0.5% (w/v) hydroxypropyl methylcellulose and 0.4% (v/v) in Milli-Q H₂O. Blood samples (10 µl) were collected from the tail vein of each animal at defined intervals then placed into 1.2 mL cryovials containing deionized water (90 µl) and stored at -80°C until analysis. Blood levels of DMU759 in mouse blood were determined by UPLC-MS/MS, as previously described (58).

Plasma protein binding

The propensity of DMU759 to bind to plasma proteins was determined as previously described (21).

Statistical analysis

EC₅₀ curves for *in vitro* drug sensitivity assays were plotted using two-parameter non-linear regression. Where weighted means are reported, final values are generated from at least three biological replicates with each biological replicate comprised of two technical replicates. ActivityBase (IDBS, version 8.0.5.4) was used to analyze data generated from *TcKRS1* and human KRS enzyme inhibition assays. Percentage inhibition curves were fitted to a four-parameter logistic dose-response equation (XLfit model 203), with pre-fitting for all four parameters. IC₅₀ values represent the geometric mean with 95% confidence intervals determined from at least three biological replicates (n = 3). The 95% confidence interval indicates the concentration range within which IC₅₀ values are likely to fall.

Supplementary materials

Supplementary materials

Figs S1 to S6

Tables S1 to S8

Data file S1

Reproducibility Checklist

- 730 1. Global age-sex-specific fertility, mortality, healthy life expectancy (HALE), and population
731 estimates in 204 countries and territories, 1950-2019: a comprehensive demographic
732 analysis for the Global Burden of Disease Study 2019. *Lancet (London, England)* **396**, 1160-
733 1203 (2020).
- 734 2. A. F. Francisco, S. Jayawardhana, M. D. Lewis, M. C. Taylor, J. M. Kelly, Biological factors that
735 impinge on Chagas disease drug development. *Parasitology* **144**, 1871-1880 (2017).
- 736 3. K. C. F. Lidani, F. A. Andrade, L. Bavia, F. S. Damasceno, M. H. Beltrame, I. J. Messias-
737 Reason, T. L. Sandri, Chagas Disease: From Discovery to a Worldwide Health Problem. *Front*
738 *Public Health* **7**, 166 (2019).
- 739 4. R. Click Lambert, K. N. Kolivras, L. M. Resler, C. C. Brewster, S. L. Paulson, The potential for
740 emergence of Chagas disease in the United States. *Geospat Health* **2**, 227-239 (2008).
- 741 5. E. Chatelain, I. Scandale, Animal models of Chagas disease and their translational value to
742 drug development. *Expert Opin Drug Discov* **15**, 1381-1402 (2020).
- 743 6. B. S. Hall, S. R. Wilkinson, Activation of benznidazole by trypanosomal type I nitroreductases
744 results in glyoxal formation. *Antimicrobial agents and chemotherapy* **56**, 115-123 (2012).
- 745 7. B. S. Hall, C. Bot, S. R. Wilkinson, Nifurtimox activation by trypanosomal type I
746 nitroreductases generates cytotoxic nitrile metabolites. *J Biol Chem* **286**, 13088-13095
747 (2011).
- 748 8. S. R. Wilkinson, M. C. Taylor, D. Horn, J. M. Kelly, I. Cheeseman, A mechanism for cross-
749 resistance to nifurtimox and benznidazole in trypanosomes. *Proceedings of the National*
750 *Academy of Sciences of the United States of America* **105**, 5022-5027 (2008).
- 751 9. J. A. Castro, M. M. de Mecca, L. C. Bartel, Toxic side effects of drugs used to treat Chagas'
752 disease (American trypanosomiasis). *Hum Exp Toxicol* **25**, 471-479 (2006).
- 753 10. C. Bern, Antitrypanosomal therapy for chronic Chagas' disease. *N Engl J Med* **364**, 2527-2534
754 (2011).
- 755 11. I. Molina, J. Gómez i Prat, F. Salvador, B. Treviño, E. Sulleiro, N. Serre, D. Pou, S. Roure, J.
756 Cabezas, L. Valerio, A. Blanco-Grau, A. Sánchez-Montalvá, X. Vidal, A. Pahissa, Randomized
757 trial of posaconazole and benznidazole for chronic Chagas' disease. *N Engl J Med* **370**, 1899-
758 1908 (2014).
- 759 12. J. A. Urbina, G. Payares, L. M. Contreras, A. Liendo, C. Sanoja, J. Molina, M. Piras, R. Piras, N.
760 Perez, P. Wincker, D. Loebenberg, Antiproliferative effects and mechanism of action of SCH
761 56592 against *Trypanosoma* (*Schizotrypanum*) *cruzi*: in vitro and in vivo studies.
762 *Antimicrobial agents and chemotherapy* **42**, 1771-1777 (1998).
- 763 13. J. Molina, O. Martins-Filho, Z. Brener, A. J. Romanha, D. Loebenberg, J. A. Urbina, Activities
764 of the triazole derivative SCH 56592 (posaconazole) against drug-resistant strains of the
765 protozoan parasite *Trypanosoma* (*Schizotrypanum*) *cruzi* in immunocompetent and
766 immunosuppressed murine hosts. *Antimicrobial agents and chemotherapy* **44**, 150-155
767 (2000).
- 768 14. V. Kande Betu Kumesu, W. Mutombo Kalonji, C. Bardonneau, O. Valverde Mordt, D. Ngolo
769 Tete, S. Blesson, F. Simon, S. Delhomme, S. Bernhard, P. Nganzobo Ngima, H. Mahenzi
770 Mbembo, J. P. Fina Lubaki, S. Lumeya Vuvu, W. Kuziena Mindele, M. Ilunga Wa Kyhi, G.
771 Mandula Mokenge, L. Kaninda Badibabi, A. Kasongo Bonama, P. Kavunga Lukula, C.
772 Lumbala, B. Scherrer, N. Strub-Wourgaft, A. Tarral, Safety and efficacy of oral fexinidazole in
773 children with gambiense human African trypanosomiasis: a multicentre, single-arm, open-
774 label, phase 2-3 trial. *The Lancet. Global health* **10**, e1665-e1674 (2022).

15. L. M. MacLean, J. Thomas, M. D. Lewis, I. Cotillo, D. W. Gray, M. De Rycker, Development of Trypanosoma cruzi in vitro assays to identify compounds suitable for progression in Chagas' disease drug discovery. *PLoS neglected tropical diseases* **12**, e0006612 (2018).
16. M. De Rycker, J. Thomas, J. Riley, S. J. Brough, T. J. Miles, D. W. Gray, Identification of Trypanocidal Activity for Known Clinical Compounds Using a New Trypanosoma cruzi Hit-Discovery Screening Cascade. *PLoS neglected tropical diseases* **10**, e0004584 (2016).
17. A. F. Francisco, M. D. Lewis, S. Jayawardhana, M. C. Taylor, E. Chatelain, J. M. Kelly, Limited Ability of Posaconazole To Cure both Acute and Chronic Trypanosoma cruzi Infections Revealed by Highly Sensitive In Vivo Imaging. *Antimicrobial agents and chemotherapy* **59**, 4653-4661 (2015).
18. A. S. Bhambra, M. Edgar, M. R. J. Elsegood, Y. Li, G. W. Weaver, R. R. J. Arroo, V. Yardley, H. Burrell-Saward, V. Krystof, Design, synthesis and antitrypanosomal activities of 2,6-disubstituted-4,5,7-trifluorobenzothiophenes. *European journal of medicinal chemistry* **108**, 347-353 (2016).
19. R. J. Wall, E. Rico, I. Lukac, F. Zuccotto, S. Elg, I. H. Gilbert, Y. Freund, M. R. K. Alley, M. C. Field, S. Wyllie, D. Horn, Clinical and veterinary trypanocidal benzoxaboroles target CPSF3. *Proceedings of the National Academy of Sciences of the United States of America* **115**, 9616-9621 (2018).
20. J. C. Hanna, V. Corpas-Lopez, S. Seizova, B. L. Colon, R. Bacchetti, G. M. J. Hall, E. M. Sands, L. Robinson, B. Baragaña, S. Wyllie, M. C. Pawlowic, Mode of action studies confirm on-target engagement of lysyl-tRNA synthetase inhibitor and lead to new selection marker for Cryptosporidium. *Front Cell Infect Microbiol* **13**, 1236814 (2023).
21. B. Baragaña, B. Forte, R. Choi, S. Nakazawa Hewitt, J. A. Bueren-Calabuig, J. P. Pisco, C. Peet, D. M. Dranow, D. A. Robinson, C. Jansen, N. R. Norcross, S. Vinayak, M. Anderson, C. F. Brooks, C. A. Cooper, S. Damerow, M. Delves, K. Dowers, J. Duffy, T. E. Edwards, I. Hallyburton, B. G. Horst, M. A. Hulverson, L. Ferguson, M. B. Jiménez-Díaz, R. S. Jumani, D. D. Lorimer, M. S. Love, S. Maher, H. Matthews, C. W. McNamara, P. Miller, S. O'Neill, K. K. Ojo, M. Osuna-Cabello, E. Pinto, J. Post, J. Riley, M. Rottmann, L. M. Sanz, P. Scullion, A. Sharma, S. M. Shepherd, Y. Shishikura, F. R. C. Simeons, E. E. Stebbins, L. Stojanovski, U. Straschil, F. K. Tamaki, J. Tamjar, L. S. Torrie, A. Vantaux, B. Witkowski, S. Wittlin, M. Yogavel, F. Zuccotto, I. Angulo-Barturen, R. Sinden, J. Baum, F. J. Gamo, P. Mäser, D. E. Kyle, E. A. Winzeler, P. J. Myler, P. G. Wyatt, D. Floyd, D. Matthews, A. Sharma, B. Striepen, C. D. Huston, D. W. Gray, A. H. Fairlamb, A. V. Pisliakov, C. Walpole, K. D. Read, W. C. Van Voorhis, I. H. Gilbert, Lysyl-tRNA synthetase as a drug target in malaria and cryptosporidiosis. *Proceedings of the National Academy of Sciences of the United States of America* **116**, 7015-7020 (2019).
22. S. R. Green, S. H. Davis, S. Damerow, C. A. Engelhart, M. Mathieson, B. Baragaña, D. A. Robinson, J. Tamjar, A. Dawson, F. K. Tamaki, K. I. Buchanan, J. Post, K. Dowers, S. M. Shepherd, C. Jansen, F. Zuccotto, I. H. Gilbert, O. Epemolu, J. Riley, L. Stojanovski, M. Osuna-Cabello, E. Pérez-Herrán, M. J. Rebollo, L. Guijarro López, P. Casado Castro, I. Camino, H. C. Kim, J. M. Bean, N. Nahiyaan, K. Y. Rhee, Q. Wang, V. Y. Tan, H. I. M. Boshoff, P. J. Converse, S. Y. Li, Y. S. Chang, N. Fotouhi, A. M. Upton, E. L. Nuermberger, D. Schnappinger, K. D. Read, L. Encinas, R. H. Bates, P. G. Wyatt, L. A. T. Cleghorn, Lysyl-tRNA synthetase, a target for urgently needed M. tuberculosis drugs. *Nat Commun* **13**, 5992 (2022).
23. S. N. Hewitt, D. M. Dranow, B. G. Horst, J. A. Abendroth, B. Forte, I. Hallyburton, C. Jansen, B. Baragaña, R. Choi, K. L. Rivas, M. A. Hulverson, M. Dumais, T. E. Edwards, D. D. Lorimer, A. H. Fairlamb, D. W. Gray, K. D. Read, A. M. Lehane, K. Kirk, P. J. Myler, A. Wernimont, C. Walpole, R. Stacy, L. K. Barrett, I. H. Gilbert, W. C. Van Voorhis, Biochemical and Structural

- Characterization of Selective Allosteric Inhibitors of the Plasmodium falciparum Drug Target, Prolyl-tRNA-synthetase. *ACS infectious diseases* **3**, 34-44 (2017).
24. Y. Español, D. Thut, A. Schneider, L. Ribas de Pouplana, A mechanism for functional segregation of mitochondrial and cytosolic genetic codes. *Proceedings of the National Academy of Sciences of the United States of America* **106**, 19420-19425 (2009).
25. R. Milne, N. Wiedemar, V. Corpas-Lopez, E. Moynihan, R. J. Wall, A. Dawson, D. A. Robinson, S. M. Shepherd, R. J. Smith, I. Hallyburton, J. M. Post, K. Dowers, L. S. Torrie, I. H. Gilbert, B. Baragaña, S. Patterson, S. Wyllie, Toolkit of Approaches To Support Target-Focused Drug Discovery for Plasmodium falciparum Lysyl tRNA Synthetase. *ACS infectious diseases* **8**, 1962-1974 (2022).
26. S. Altmann, E. Rico, S. Carvalho, M. Ridgway, A. Trenaman, H. Donnelly, M. Tinti, S. Wyllie, D. Horn, Oligo targeting for profiling drug resistance mutations in the parasitic trypanosomatids. *Nucleic acids research* **50**, e79 (2022).
27. T. Beneke, R. Madden, L. Makin, J. Valli, J. Sunter, E. Gluenz, A CRISPR Cas9 high-throughput genome editing toolkit for kinetoplastids. *Royal Society open science* **4**, 170095 (2017).
28. A. H. Fairlamb, S. Wyllie, The critical role of mode of action studies in kinetoplastid drug discovery. *Frontiers in Drug Discovery* **3**, 1185679 (2023).
29. M. L. Lima, L. B. Tulloch, V. Corpas-Lopez, S. Carvalho, R. J. Wall, R. Milne, E. Rico, S. Patterson, I. H. Gilbert, S. Moniz, L. MacLean, L. S. Torrie, C. Morgillo, D. Horn, F. Zuccotto, S. Wyllie, Identification of a Proteasome-Targeting Arylsulfonamide with Potential for the Treatment of Chagas' Disease. *Antimicrobial agents and chemotherapy* **66**, e0153521 (2022).
30. M. C. Taylor, A. I. Ward, F. Olmo, A. F. Francisco, S. Jayawardhana, F. C. Costa, M. D. Lewis, J. M. Kelly, Bioluminescent:Fluorescent Trypanosoma cruzi Reporter Strains as Tools for Exploring Chagas Disease Pathogenesis and Drug Activity. *Curr Pharm Des* **27**, 1733-1740 (2021).
31. M. D. Lewis, A. Fortes Francisco, M. C. Taylor, H. Burrell-Saward, A. P. McLatchie, M. A. Miles, J. M. Kelly, Bioluminescence imaging of chronic Trypanosoma cruzi infections reveals tissue-specific parasite dynamics and heart disease in the absence of locally persistent infection. *Cell Microbiol* **16**, 1285-1300 (2014).
32. A. F. Francisco, S. Jayawardhana, M. D. Lewis, K. L. White, D. M. Shackleford, G. Chen, J. Saunders, M. Osuna-Cabello, K. D. Read, S. A. Charman, E. Chatelain, J. M. Kelly, Nitroheterocyclic drugs cure experimental Trypanosoma cruzi infections more effectively in the chronic stage than in the acute stage. *Scientific reports* **6**, 35351 (2016).
33. E. V. Smirnova, V. A. Lakunina, I. Tarassov, I. A. Krashennnikov, P. A. Kamenski, Noncanonical functions of aminoacyl-tRNA synthetases. *Biochemistry (Mosc)* **77**, 15-25 (2012).
34. C. S. Francklyn, P. Mullen, Progress and challenges in aminoacyl-tRNA synthetase-based therapeutics. *J Biol Chem* **294**, 5365-5385 (2019).
35. J. M. Kratz, Drug discovery for chagas disease: A viewpoint. *Acta Trop* **198**, 105107 (2019).
36. M. Cal, J. R. Ioset, M. A. Fügi, P. Mäser, M. Kaiser, Assessing anti-T. cruzi candidates in vitro for sterile cidal activity. *Int J Parasitol Drugs Drug Resist* **6**, 165-170 (2016).
37. N. Trometer, J. Pecourneau, L. Feng, J. A. Navarro-Huerta, D. Lazarin-Bidóia, S. de Oliveira Silva Lautenschlager, L. Maes, A. Fortes Francisco, J. M. Kelly, B. Meunier, M. Cal, P. Mäser, M. Kaiser, E. Davioud-Charvet, Synthesis and Anti-Chagas Activity Profile of a Redox-Active Lead 3-Benzylmenadione Revealed by High-Content Imaging. *ACS infectious diseases* **10**, 1808-1838 (2024).

38. H. Hirumi, K. Hirumi, Continuous cultivation of *Trypanosoma brucei* blood stream forms in a medium containing a low concentration of serum protein without feeder cell layers. *J Parasitol* **75**, 985-989 (1989).
39. S. Goyard, H. Segawa, J. Gordon, M. Showalter, R. Duncan, S. J. Turco, S. M. Beverley, An in vitro system for developmental and genetic studies of *Leishmania donovani* phosphoglycans. *Mol Biochem Parasitol* **130**, 31-42 (2003).
40. N. C. Ammerman, M. Beier-Sexton, A. F. Azad, Growth and maintenance of Vero cell lines. *Curr Protoc Microbiol* **Appendix 4**, Appendix 4E (2008).
41. D. C. Jones, I. Hallyburton, L. Stojanovski, K. D. Read, J. A. Frearson, A. H. Fairlamb, Identification of a κ -opioid agonist as a potent and selective lead for drug development against human African trypanosomiasis. *Biochem Pharmacol* **80**, 1478-1486 (2010).
42. N. Vahekeni, T. Brillatz, M. Rahmaty, M. Cal, S. Keller-Maerki, R. Rocchetti, M. Kaiser, S. Sax, K. Mattli, E. Wolfram, L. Marcourt, E. F. Queiroz, J. L. Wolfender, P. Mäser, Antiprotozoal Activity of Plants Used in the Management of Sleeping Sickness in Angola and Bioactivity-Guided Fractionation of *Brasenia schreberi* J.F.Gmel and *Nymphaea lotus* L. Active against *T. b. rhodesiense*. *Molecules* **29**, (2024).
43. S. Wyllie, S. Patterson, L. Stojanovski, F. R. Simeons, S. Norval, R. Kime, K. D. Read, A. H. Fairlamb, The anti-trypanosome drug fexinidazole shows potential for treating visceral leishmaniasis. *Science translational medicine* **4**, 119re111 (2012).
44. A. Prjibelski, D. Antipov, D. Meleshko, A. Lapidus, A. Korobeynikov, Using SPAdes De Novo Assembler. *Curr Protoc Bioinformatics* **70**, e102 (2020).
45. M. Mirdita, M. Steinegger, J. Söding, MMseqs2 desktop and local web server app for fast, interactive sequence searches. *Bioinformatics* **35**, 2856-2858 (2019).
46. H. A. Lorenzi, M. P. Vazquez, M. J. Levin, Integration of expression vectors into the ribosomal locus of *Trypanosoma cruzi*. *Gene* **310**, 91-99 (2003).
47. S. Alsford, T. Kawahara, L. Glover, D. Horn, Tagging a *T. brucei* RRNA locus improves stable transfection efficiency and circumvents inducible expression position effects. *Mol Biochem Parasitol* **144**, 142-148 (2005).
48. L. B. Tulloch, M. Tinti, R. J. Wall, S. K. Weidt, V. Corpas-Lopez, G. Dey, T. K. Smith, A. H. Fairlamb, M. P. Barrett, S. Wyllie, Sterol 14- α demethylase (CYP51) activity in *Leishmania donovani* is likely dependent upon cytochrome P450 reductase 1. *PLoS pathogens* **20**, e1012382 (2024).
49. L. S. Paradela, R. J. Wall, S. Carvalho, G. Chemi, V. Corpas-Lopez, E. Moynihan, D. Bello, S. Patterson, M. L. S. Güther, A. H. Fairlamb, M. A. J. Ferguson, F. Zuccotto, J. Martin, I. H. Gilbert, S. Wyllie, Multiple unbiased approaches identify oxidosqualene cyclase as the molecular target of a promising anti-leishmanial. *Cell chemical biology* **28**, 711-721.e718 (2021).
50. G. Winter, J. Beilsten-Edmands, N. Devenish, M. Gerstel, R. J. Gildea, D. McDonagh, E. Pascal, D. G. Waterman, B. H. Williams, G. Evans, DIALS as a toolkit. *Protein Sci* **31**, 232-250 (2022).
51. P. R. Evans, G. N. Murshudov, How good are my data and what is the resolution? *Acta Crystallogr D Biol Crystallogr* **69**, 1204-1214 (2013).
52. A. J. McCoy, R. W. Grosse-Kunstleve, P. D. Adams, M. D. Winn, L. C. Storoni, R. J. Read, Phaser crystallographic software. *J Appl Crystallogr* **40**, 658-674 (2007).
53. P. Emsley, B. Lohkamp, W. G. Scott, K. Cowtan, Features and development of Coot. *Acta Crystallogr D Biol Crystallogr* **66**, 486-501 (2010).

- 916 54. G. N. Murshudov, P. Skubák, A. A. Lebedev, N. S. Pannu, R. A. Steiner, R. A. Nicholls, M. D.
917 Winn, F. Long, A. A. Vagin, REFMAC5 for the refinement of macromolecular crystal
918 structures. *Acta Crystallogr D Biol Crystallogr* **67**, 355-367 (2011).
- 919 55. M. D. Winn, C. C. Ballard, K. D. Cowtan, E. J. Dodson, P. Emsley, P. R. Evans, R. M. Keegan,
920 E. B. Krissinel, A. G. Leslie, A. McCoy, S. J. McNicholas, G. N. Murshudov, N. S. Pannu, E. A.
921 Potterton, H. R. Powell, R. J. Read, A. Vagin, K. S. Wilson, Overview of the CCP4 suite and
922 current developments. *Acta Crystallogr D Biol Crystallogr* **67**, 235-242 (2011).
- 923 56. F. Long, R. A. Nicholls, P. Emsley, S. Graëulis, A. Merkys, A. Vaitkus, G. N. Murshudov,
924 AceDRG: a stereochemical description generator for ligands. *Acta Crystallogr D Struct Biol*
925 **73**, 112-122 (2017).
- 926 57. C. J. Williams, J. J. Headd, N. W. Moriarty, M. G. Prisant, L. L. Videau, L. N. Deis, V. Verma, D.
927 A. Keedy, B. J. Hintze, V. B. Chen, S. Jain, S. M. Lewis, W. B. Arendall, 3rd, J. Snoeyink, P. D.
928 Adams, S. C. Lovell, J. S. Richardson, D. C. Richardson, MolProbity: More and better
929 reference data for improved all-atom structure validation. *Protein Sci* **27**, 293-315 (2018).
- 930 58. S. González, R. J. Wall, J. Thomas, S. Brailard, G. Brunori, I. Camino Díaz, J. Cantizani, S.
931 Carvalho, P. Castañeda Casado, E. Chatelain, I. Cutillo, J. M. Fiandor, A. F. Francisco, D.
932 Grimsditch, M. Keenan, J. M. Kelly, A. Kessler, C. Luise, J. J. Lyon, L. MacLean, M. Marco, J. J.
933 Martin, M. S. Martinez Martinez, C. Paterson, K. D. Read, A. Santos-Villarejo, F. Zuccotto, S.
934 Wyllie, T. J. Miles, M. De Rycker, Short-course combination treatment for experimental
935 chronic Chagas disease. *Science translational medicine* **15**, eadg8105 (2023).
- 936 59. Y. Perez-Riverol, J. Bai, C. Bandla, D. García-Seisdedos, S. Hewapathirana, S.
937 Kamatchinathan, D. J. Kundu, A. Prakash, A. Frericks-Zipper, M. Eisenacher, M. Walzer, S.
938 Wang, A. Brazma, J. A. Vizcaíno, The PRIDE database resources in 2022: a hub for mass
939 spectrometry-based proteomics evidences. *Nucleic acids research* **50**, D543-d552 (2022).

ACKNOWLEDGEMENTS

The authors would like to thank Jennnifer Riley and other members of Kevin Read's laboratory for help with plasma protein binding studies. The authors would also like to thank Diamond Light Source (proposal mx26793; beamline I04) for beamtime, and the staff at the beamline for assistance with crystal testing and data collection.

Funding: This study was supported by the Wellcome Trust (204672, 100194, 203134, 105021, and 218448). Financial support and facilities enabling chemistry development were provided by De Montfort and Loughborough Universities. The Drugs for Neglected Diseases initiative (DNDi) is grateful to its donors, public and private, who have provided funding to DNDi since its inception in 2003. A full list of DNDi's donors can be found at <http://www.dndi.org/about/donors/>. JMK acknowledges funding from DNDi.

Author contributions: HT and AET synthesized compounds. ASB, GWW, WJR, PS and BP oversaw compound design. SC and RJW performed the *T. brucei* genome-wide overexpression library screen and analysis. LBT, MLL and JD generated transgenic cell lines. LBT, MLL, JD, and MC performed *in vitro* drug sensitivity assays. VCL and GD performed proteomic assays and analysis. AFF and JMK designed and performed *in vivo* studies. LF performed DMPK assays and analysis. DR cloned and produced recombinant KRS1. LGM and LST performed enzyme assays and analysis. AD generated and solved x-ray crystal structures. LBT, SW, ASB, SC, RJW, MLL, JD, VCL, GD, LF, LGM, LST, AD, MT, SP, MC, PM, MK, JK, DR, GWW, WJR, and AFF analyzed data. LBT, SW, AFF, AD and VCL visualized the data. LBT, SW and ASB wrote the original draft. LBT, SW, ASB, SC, RJW, MLL, VCL, AD, PM, JK, AFF, and LST reviewed

and edited the manuscript. **SW and ASB** managed and coordinated the project and obtained funding.

Competing interests: ASB and GWW are co-inventors on Patent Cooperation Treaty patent application number **PCT/GB2024/050205** and UK patent application number **GB2301138.0**, entitled “5,6,8- Trifluoroquinazolines to treat parasitic infection”, which covers the two compounds presented in this study. The other authors declare no competing interests.

Data and Materials Availability: All data are available in the main text or supplementary materials. Mass spectrometry datasets have been deposited to the ProteomeXchange Consortium through the PRIDE (59) partner repository under the dataset identifier PXD050235. Genome-wide overexpression library datasets have been deposited in the National Centre for Biotechnology Information Sequence Read Archive (NCBI SRA) under project code PRJNA1076710. The coordinates and reflections file for crystallographic studies demonstrating DMU371 bound to *TcCpKRS1* and lysine were submitted to the Protein Data Bank with the accession code 8S0V. DMU371 and DMU759 can be provided via an MTA by contacting ASB.

Supplementary Materials

Anti-trypanosomal quinazolines target lysyl-tRNA-synthetases and demonstrate partial efficacy in a model of acute Chagas infection

This file includes:

Supplementary materials and methods

Chemical synthesis

Tetrafluorinated intermediates (DMU371-I and DMU759-I)

4-(cyclopentylamino)-2,3,5,6-tetrafluorobenzonitrile (DMU371-I)

4-(cyclohexanethio)-2,3,5,6-tetrafluorobenzonitrile (DMU759-I)

Synthesis of DMU371 and DMU759

N7-Cyclopentyl-5,6,8-trifluoro-2-methylquinazoline-4,7-diamine (DMU371)

7-(Cyclohexylthio)-5,6,8-trifluoro-2-methylquinazolin-4-amine (DMU759)

DMPK assays

Metabolic stability

In vitro CYP inhibition

In vitro hERG fluorescence polarization assay

Supplementary figures

Fig.S1. Schematic representation of the two-step aaRS reaction scheme (black arrows).

Fig.S2. Amino acid sequence similarity matrix (%) for a range of kinetoplastid, apicomplexan, bacterial and human KRS enzymes.

Fig.S3. Relative KRS1 protein levels in selected WT and transgenic *T. brucei*, *T. cruzi* and *L. donovani* cell lines.

Fig.S4. Alignment of *T. cruzi*, *C. parvum* and *P. falciparum* KRS1 genes.

Fig.S5. Crystal structure of the *TcCpKRS* active site with bound lysine and DMU371.

Fig. S6. Pharmacokinetic properties of DMU759.

Supplementary tables

Table S1: Collated EC₅₀ values for WT and transgenic kinetoplastid cell lines.

Table S2: *In vitro* ADME profile of DMU371 and DMU759.

Table S3: Fragment hits from screening the *T. brucei* overexpression library with DMU371.

Table S4: Collated EC₅₀ values for established KRS1 inhibitor DDD01510706 against WT and transgenic kinetoplastid cell lines.

Table S5: Top hits from isothermal TPP with DMU371.

Table S6: Top hits from isothermal TPP with DMU759.

Table S7: Statistics for the crystal structure of *TcCp*KRS1 with bound DMU371 and lysine.

Table S8: Primers used in this study.

Supplementary materials and methods

Chemical syntheses

Tetrafluorinated intermediates (DMU371-I and DMU759-I) - Pentafluorobenzonitrile (1.00 g, 5.18 mmol) and triethylamine (1.31 g, 12.95 mmol) were dissolved in THF followed by the addition of either cyclopentylamine or cyclohexanethiol (5.18 mmol). The mixture was stirred at RT for 12 h and subsequently quenched with water (100 ml). The crude product was extracted with ethyl acetate (3 × 50 ml). The combined organic extracts were dried over MgSO₄ and the solvent removed under vacuum. The crude product was recrystallised using EtOH to afford desired tetrafluorinated intermediates.

4-(cyclopentylamino)-2,3,5,6-tetrafluorobenzonitrile (DMU371-I) - Yellow solid: (0.94 g, 70%); mp 107 – 109 °C; ¹H-NMR (600 MHz, CDCl₃) δ 4.34 (s, 1H), 4.29 — 4.22 (m, 1H), 2.08 — 2.03 (m, 2H), 1.78 — 1.72 (m, 2H), 1.70 — 1.63 (m, 2H), 1.54 — 1.49 (m, 2H); ¹³C-NMR (151 MHz, CDCl₃) δ 149.0 — 147.2 (m), 136.4 — 134.9 (m), 133.2 — 133.0 (m), 109.1 (t, J = 3.3 Hz), 78.7 (t, J = 17.7 Hz), 56.6 (t, J = 3.6 Hz), 34.8, 23.7; ¹⁹F-NMR (565 MHz, CDCl₃) δ -135.5 (td, J = 17.6, 11.2 Hz, 2F), -159.9 (d, J = 14.1 Hz, 2F); HRMS: m/z found: 259.0862 C₁₂H₁₀F₄N₂ [M+H]⁺ requires 259.0858.

4-(cyclohexanethio)-2,3,5,6-tetrafluorobenzonitrile (DMU759-I) - White solid: (1.39 g, 93%); mp 98 – 100 °C; ¹H-NMR (600 MHz, CDCl₃) δ 3.50 – 3.45 (m, 1H), 1.92 – 1.89 (m, 2H), 1.81 – 1.77 (m, 2H), 1.63 (td, J = 8.2, 4.0 Hz, 1H), 1.43 – 1.22 (m, 5H); ¹³C-NMR (151 MHz, CDCl₃) δ 147.9 — 147.4 (m), 146.2 — 145.7 (m), 123.2 (t, J = 19.9 Hz), 107.6 (t, J = 3.6 Hz), 93.0 — 92.7 (m), 47.3, 33.6, 25.8, 25.4; ¹⁹F-NMR (565 MHz, CDCl₃) δ -130.4 (q, J = 9.9 Hz, 2F), -132.6 (q, J = 11.3 Hz, 2F); HRMS: m/z found: 290.0627 C₁₃H₁₁F₄NS [M+H]⁺ requires 290.0627.

Synthesis of DMU371 and DMU759

The relevant tetrafluorinated intermediate (1.76 mmol), 1,8-diazabicyclo[5.4.0]undec-7-ene (DBU, 0.671 g, 4.41 mmol) and acetamidinium chloride (0.166 g, 1.76 mmol) were dissolved in DMF (3 ml) and stirred under reflux for 15 h. The reaction was quenched with water (100 ml) and the crude product extracted with DCM (dichloromethane, 3 × 15 ml). The combined extracts were dried over MgSO₄ and the solvent evaporated under vacuum. The product was purified using column chromatography (elution with DCM/MeOH).

N7-Cyclopentyl-5,6,8-trifluoro-2-methylquinazoline-4,7-diamine (DMU371) - White solid: (0.177 g, 34%); mp 231 – 233 °C; ¹H-NMR (600 MHz, CDCl₃) δ 5.81 (s, 2H), 4.34 (d, J = 7.6 Hz, 1H), 4.13 (t, J = 3.4 Hz, 1H), 2.57 (s, 3H), 2.09 — 2.03 (m, 2H), 1.78-1.71 (m, 2H), 1.68 — 1.63 (m, 2H), 1.53 (dt, J = 19.0, 6.5 Hz, 2H); ¹³C-NMR (151 MHz, CDCl₃) δ 165.2, 158.6, 143.9 — 142.2 (m), 140.6 — 138.7 (m), 138.1 (d, J = 11.6 Hz), 137.3 (m), 130.5 (td, J = 12.1, 3.4 Hz), 93.6 (dd, J = 10.1, 2.9 Hz), 56.7, 34.7, 26.4, 23.8; ¹⁹F-NMR (565 MHz, CDCl₃) δ -145.5 (m, 1F), -151.9 (m, 1F), -157.2 (dt, J = 20.7, 3.7 Hz, 1F); HRMS: m/z found: 297.1325 C₁₄H₁₅F₃N₄ [M+H]⁺ requires 297.1322.

7-(Cyclohexylthio)-5,6,8-trifluoro-2-methylquinazolin-4-amine (DMU759) - Yellow solid: 0.150 g (26%); mp 194 – 196 °C; ¹H-NMR (600 MHz, CDCl₃) δ 6.04 (s, 2H), 3.44 (s, 1H), 2.63 (s, 3H), 1.92 (d, J = 10.6 Hz, 2H), 1.76 (s, 2H), 1.6 (1H, overlapped by H₂O), 1.40 (d, J = 10.6 Hz, 2H), 1.31 — 1.22 (m, 3H); ¹³C{¹H,¹⁹F}-NMR (125 MHz, CDCl₃) δ 165.6, 158.7, 153.6, 145.4, 142.1, 137.8, 117.9, 103.1, 47.0, 33.6, 26.4, 25.9, 25.5; ¹⁹F-NMR (565 MHz, CDCl₃) δ -118.9 (d, J = 17.0 Hz, 1F), -134.4 (d, J = 25.4 Hz, 1F), -143.9 (t, J = 21.2 Hz, 1F); HRMS: m/z found: 328.1094 C₁₅H₁₆F₃N₃S [M+H]⁺ requires 328.1090.

DMPK assays

Metabolic stability

The metabolic stability of key compounds was assessed using the protocol established by TCG Lifesciences (India). Briefly, mouse liver microsomes (MLM) were incubated with test compounds or controls (atenolol, propranolol, diclofenac and verapamil) at 1 μ M. Reactions were initiated by the addition of NADPH and terminated by the addition of acetonitrile. Metabolism of test and control compounds at 5 different time-points was monitored via LC/MS/MS.

***In vitro* CYP inhibition**

Compounds were screened for CYP inhibition activity using the protocol established by TCG Lifesciences (India). The activity of five CYP450 isoforms: 1A2; 2C9; 2D6, 3A4; and 2C19 was monitored in the presence of test or control (miconazole) compounds at 10 μ M. Reactions were terminated after 10 min (30 min for CYP2C19) by the addition of acetonitrile, centrifuged and analysed via LC-MS/MS.

***In vitro* hERG fluorescence polarization assay**

Compounds were assessed for potential hERG channel inhibition using the Predictor® hERG Fluorescence Polarization Assay Kit (Invitrogen), as per manufacturer's instructions. Compounds were screened with test compounds at concentrations ranging from 0.0003 – 30 μ M. Fluorescence polarization was measured using EnVision plate reader fitted with polarized filters (excitation: 531 nm; emission: 595 nm). IC₅₀ values were determined using GraphPad Prism software.

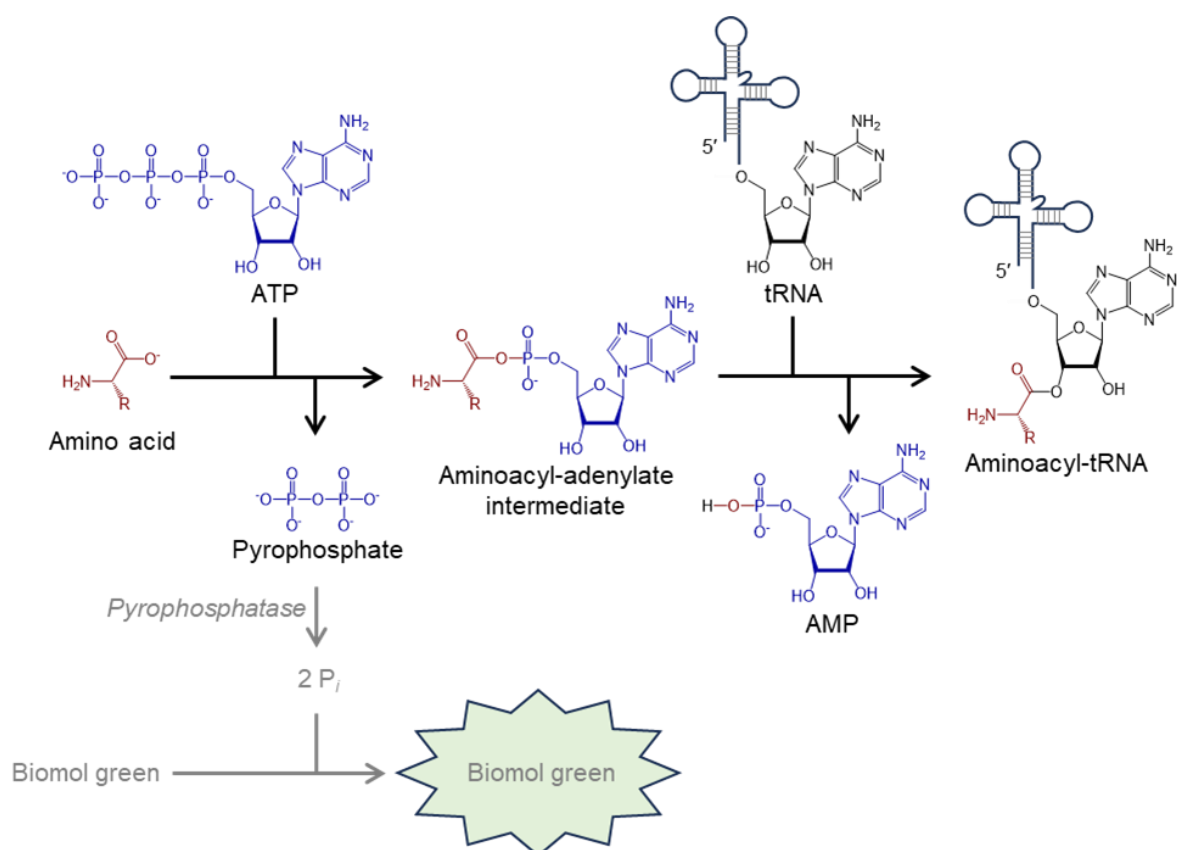


Fig. S1: Schematic representation of the two-step aaRS reaction scheme (black arrows).

The coupled pyrophosphatase/BIOMOL® Green assay used to measure recombinant KRS1 enzymatic activity indicated in grey arrows.

	<i>Tc</i> KRS1	<i>Tb</i> KRS1	<i>Ld</i> KRS1	<i>Pf</i> KRS1	<i>Cp</i> KRS	<i>Hs</i> KRS1	<i>Tc</i> KRS2	<i>Tb</i> KRS2	<i>Ld</i> KRS2	<i>Mt</i> KRS
<i>Tc</i> KRS1	100	75	73	44	47	48	35	35	36	36
<i>Tb</i> KRS1	75	100	70	44	47	51	32	33	36	34
<i>Ld</i> KRS1	73	70	100	44	47	47	36	35	38	34
<i>Pf</i> KRS1	44	44	44	100	51	51	35	37	42	33
<i>Cp</i> KRS	47	47	47	51	100	53	35	37	40	34
<i>Hs</i> KRS1	48	51	47	51	53	100	34	36	41	35
<i>Tc</i> KRS2	35	32	36	35	35	34	100	68	64	34
<i>Tb</i> KRS2	35	33	35	37	37	36	68	100	65	34
<i>Ld</i> KRS2	36	36	38	42	40	41	64	65	100	37
<i>Mt</i> KRS	36	34	34	33	34	35	34	34	37	100

Fig. S2: Amino acid sequence similarity matrix (%) for a range of kinetoplastid, apicomplexan, bacterial and human KRS enzymes. The matrix was generated via sequence alignment using Clustal-Omega (version 1.2.4). Gene IDs as follows: *Tb*KRS1 (Tb927.8.1600); *Ld*KRS1 (LdBPK_150270), *Pf*KRS1 (XP_001350214.1), *Cp*KRS1 (XP_625825.1), *Hs*KRS1 (AAG30114.1), *Tc*KRS2 (*Tc*KRS2.clone X10/7), *Tb*KRS2 (Tb927.6.1510), *Ld*KRS2 (LdBPK_300130), *Mt*KRS (WP_072520048.1).

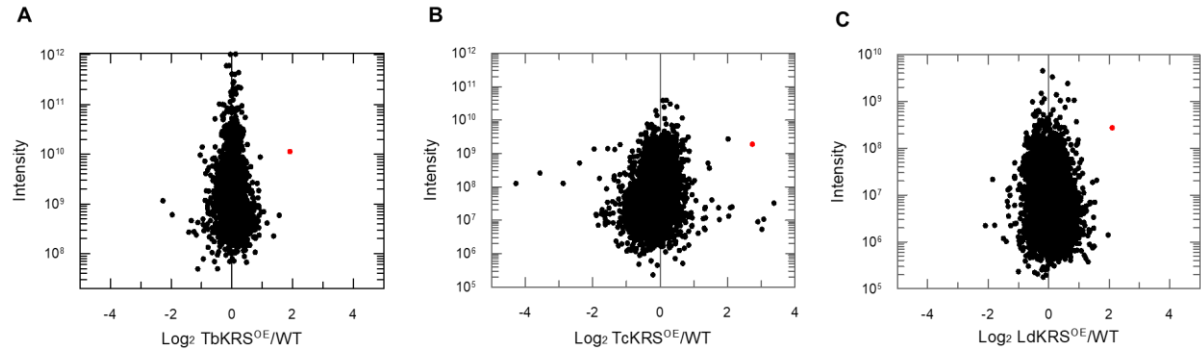


Fig. S3: Relative KRS1 protein levels in selected WT and transgenic *T. brucei*, *T. cruzi* and *L. donovani* cell lines. Protein levels (relative to WT) were determined by label-free quantitation. KRS1 relative expression in *T. brucei* (A), *T. cruzi* (B) and *L. donovani* (C) highlighted in red. Details of these analyses can be found in the Materials and Methods.

TcKRS1 MSS-----TNETRAQIDD-LAAAIAQV--KKEKGAASEEC 32
PfKRS1 MTSKSFLLSFLKYKHVNTYIFEKSFSKILKNTKKHIDCHLKSCFVTMNEKKEHVLEGEKN 60
CpKRS1 MPCLSYILAALVETIIRLLFF-----FNYFVRMST----- 30
 * . : :

TcKRS1 RALVAKMTELRKQLPAKKVEKAPELSYFDTRLAMVKELGLLG-AAYPHKFDRQYTIPAFK 91
PfKRS1 KRVVNA----SKDKKKEEEGEVDPRLYFENRSKFIQDQKDKGINPYPHKFERTISIPEFI116
CpKRS1 -----EMNNQSQISDTLDSVHYTDNRYKMMECIKDAGRPFYPHKFKISMSLPAYA 80
 : : * : * : * : * :

TcKRS1 ARFAPQLSEKGQRVEEVVAIAGRIVNKRSSGSKLNFLTLQGDAETVQVISAISD--YVDD 149
PfKRS1 EKYKDL-GNGEHLEDTILNITGRIMRVSASGQKLRFDDLVDGGEKIQVLANYSFHNHEKG 175
CpKRS1 LKYGNV-ENGYIDKDTTSLSGRVTSIRSSSSKLIFYDIFCEEQKVQIIANIMEHDISTG 139
 : : : : * : * : * : : :

TcKRS1 TFAAVHGRIRRGDIIGVKGVASLSKTGEFSMNAFEITLLSTCYHMLPDGWYGLSSIEQRF 209
PfKRS1 NFAECYDKIRRGDIVGIVGPGKSKKGELSIFPKETILLSACLHMLPMK-YGLKDEIRY 234
CpKRS1 EFSVSHSEIRRGDVVGFTGFPKSKRGELSLSFSKSVLLSPCYHMLPTAISGLKDQEVRY 199
 * : * : * : * : * : * : * : * :

TcKRS1 RQRYLDFIVNRENIQTFVTRSKVIRYIRNFFEDLDFLEVETPVLNQIAGGAAARPFITHH 269
PfKRS1 RQRYLDLLINESSRHTFVTRTKIINFLRNFLNERGFFEVEVTPMMNLIAGGANARPFITHH 294
CpKRS1 RQRYLDLMLNEESRKVFKLRSRAIKYIRNYFDRLGFLEVETPMLNMIYGGAAARPFITYH 259
 * : * : * : * : * : * : * : * :

TcKRS1 NELNQRMYLRIAPELYLKELVVGMDRVYELGKQFRNEGIDLTHNPEFTSV EAYWAYADY 329
PfKRS1 NDLDDLVLRIATELPLKMLIVGGIDKVEYLGKQFRNEGIDNTHNPEFTSCEFYWAYADY 354
CpKRS1 NELETQLYMRIAPELYLKLIVGGGLDKVEYLGKNFRNEGIDLTHNPEFTAMEFYMAYADY 319
 * : * : * : * : * : * : * : * :

TcKRS1 NDWMRTTEDLFYGLAMHHIGTPFVKYAPKDSEGNQLPEVVFNFNKPFKRLYIPELEKRM 389
PfKRS1 NDLIKWSEDFFSQLVYHLFGTYKISYNKDG PENQP---IEIDFTPPYPKVSIVEEIEKVT 411
CpKRS1 YDLMDLTEELISGLVLEIHGSLKIPYHPDGPEGKC---IEIDFTTPWKRFSFVEEIESGL 376
 * : * : * : * : * : * : * : * :

TcKRS1 NVKFPTEFESDSSNAFLRELCSKHEVECIPPLTTARLLDALISHYLEPECQ-DPTFVCDH 448
PfKRS1 NTILEQPFDSNETIEKMINIIEKHIELPNPPTAAKLLDQLASHFIENKYNDKPFIVEH 471
CpKRS1 GEKLKRPLDSQENIDFMVEMCEKHEIELPHPRTAAKLLDKLAGHFVETKCT-NPSFIIDH 435
 : : * : * : * : * : * : * :

TcKRS1 PRVMSPLAKWHRDDPQLTERFELFLNKKELCNAYTELNNPIVQREEFMKQLRNKEKGDDE 508
PfKRS1 PQIMSPAKYHRTKPGTERLEMFICGKEVLNAYTELNDPFKQKECFKLQKDKREKGDTE 531
CpKRS1 PQTMSPLAKWHREKPEMTERFELFVLGKELCNAYTELNEPLQQRKFFEQQADAKASGDVE 495
 * : * : * : * : * : * : * : * :

TcKRS1 AMDIDEGFVQALEHALPPTGGWGLGIDRLVMFLTSQANIKEVLF PAMKPETSSSLTYPP 568
PfKRS1 AAQLDSAFCTSLEYGLPPTGGGLGIDRITMFLTNKNSIKDVLFP TMRPAN----- 583
CpKRS1 ACPIDETFLALEHGLPPTGGWGLGIDRLIMFLADKNNIKEVLF PAMRNVKQNAQHSNQ 555
 * : * : * : * : * : * : * : * :

TcKRS1 GTLLNGQGVPLL 580
PfKRS1 ----- 583
CpKRS1 H---SGN----- 559

Fig. S4: Alignment of *T. cruzi*, *C. parvum* and *P. falciparum* KRS1 genes. Sequences aligned using Clustal-Omega (version 1.2.4). *C. parvum* KRS1 residues mutated to their *T. cruzi* counterparts to generate the *TcCpKRS1* hybrid enzyme are highlighted in yellow.

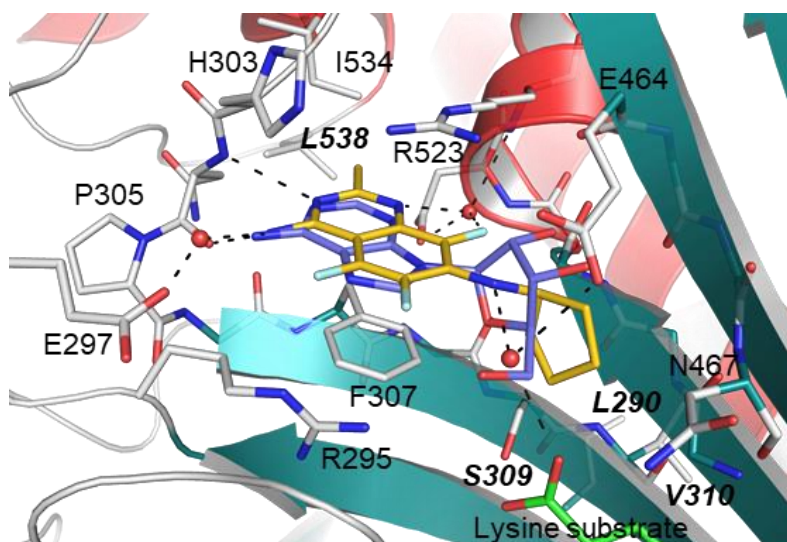


Fig. S5: Crystal structure of the *TcCpKRS* active site with bound lysine and DMU371.

Lysine represented in green and DMU371 in gold. ATP (blue) binding position taken from *HsKRS* (PDB ID: 3BJU) overlaid. Diphosphate is hidden for clarity. Key residues are labelled utilising *C. parvum* numbering, with residues mutated to *T. cruzi* counterparts in bold italics.

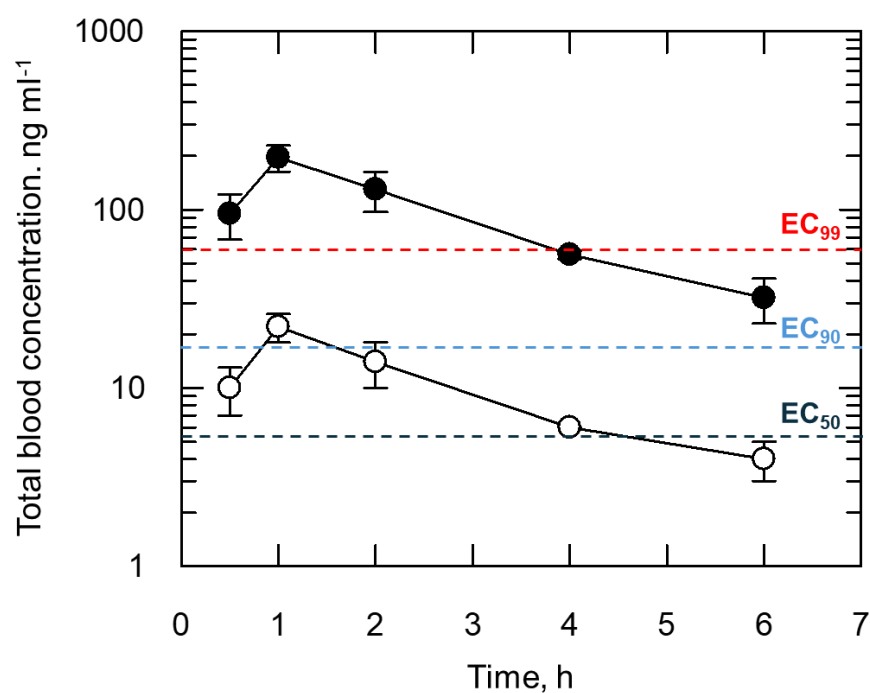
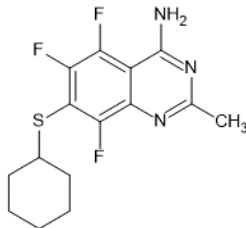
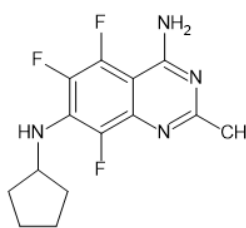


Fig. S6: Pharmacokinetic properties of DMU759. Total (black circles) and free DMU759 blood concentrations (open circles) following oral dosing (50 mg/kg). The EC₉₉ (red), EC₉₀, (blue) and EC₅₀ (dark blue) values of DMU759 for *T. cruzi* cultured in Vero cells are shown as dotted lines. Data represent the mean \pm SD from three mice.

Table S1. Collated EC₅₀ values for WT and transgenic kinetoplastid cell lines.

Organism	Cell line	Developmental stage	DMU759		DMU371	
				Fold-shift (relative to WT)		Fold-shift (relative to WT)
			EC ₅₀ value, nM		EC ₅₀ value, nM	
<i>T. b. brucei</i>	WT	BSF	112 ± 0.8	-	607 ± 9	-
	KRS1 ^{OE}		1060 ± 33	9	4250 ± 170	7
	KRS1 ^{S319L}		6480 ± 360	58	1870 ± 71	3
<i>T. b. rhodesiense</i>	WT		313 ± 183	-	1090 ± 420	-
<i>L. donovani</i> (LdBOB)	WT	Promastigote	115 ± 0.1	-	524 ± 9	-
	KRS1 ^{OE}		1470 ± 56	13	1860 ± 63	4
	KRS1 ^{S324L}		1320 ± 32	12	1740 ± 49	3
<i>L. donovani</i> (MHOM-ET-67/L82)	WT	Axenic amastigote	284 ± 20	-	5320 ± 2780	-

EC₅₀ values represent the weighted mean ± standard deviation of at least ≥2 biological replicates with each biological replicate comprised of ≥2 technical replicates. For *T. brucei rhodesiense* and *L. donovani* MHOM-ET-67/L82, EC₅₀ values represent the mean +/- standard deviation of 4 biological replicates.

Table S2: *In vitro* ADME profile of DMU371 and DMU759.

Parameter		Compound	
		DMU371	DMU759
CYP inhibition (% at 10 μM)	1A2	74.8 \pm 0.5	61.5 \pm 0.9
	2C9	8.6 \pm 0.6	7.9 \pm 0.8
	2D6	6.3 \pm 0.1	14.5 \pm 2.5
	3A4	13.0 \pm 3	0
	2C19	6.1 \pm 1.3	12.8 \pm 2.8
<i>h</i>ERG inhibition (IC₅₀ value, μM)		7.6 \pm 1.3	12.2 \pm 1.1
Mouse liver microsome stability (μl/min/mg)		>500	>500

Values represent the mean \pm standard deviation from ≥ 2 biological replicates.

Table S3: Fragment hits from screening the *T. brucei* overexpression library with DMU371. Fragments containing genes with >400 RPKM are shown. Intact reading frames shown in blue with partial or incomplete gene fragments shown in grey.

Fragment	Gene ID	Gene name	RPKM	Reads	Fragment size (kbp)	Total Reads
1	Tb927.8.1600	lysyl-tRNA synthetase, putative	221733	1501190	4.3	3,345,476
	Tb927.8.1590	ubiquitin-protein ligase, putative	9235	455976		
2	Tb927.10.4050	serine palmitoyltransferase, putative	430	2754	4.7	7,724
	Tb927.10.4060	Ankyrin repeats (3 copies), putative	426	1802		

Table S4: Collated EC₅₀ values for established KRS1 inhibitor DDD01510706 against WT and transgenic kinetoplastid cell lines.

Organism	Developmental stage	Cell line	DDD01510706	
			EC ₅₀ , μ M	Fold-shift (relative to WT)
<i>T. cruzi</i>	Epimastigote	WT	1.4 \pm 0.04	-
		KRS1 ^{OE}	13 \pm 0.4	9
		KRS1 ^{S319L}	36 \pm 4	25
<i>T. b. brucei</i>	BSF	WT	0.6 \pm 0.01	-
		KRS1 ^{OE}	3 \pm 0.1	5
		KRS1 ^{S323L}	33 \pm 1	53
<i>L. donovani</i>	Promastigote	WT	0.7 \pm 0.01	-
		KRS1 ^{OE}	8 \pm 0.5	11
		KRS1 ^{S324L}	8 \pm 0.3	12

EC₅₀ values represent the weighted mean \pm standard deviation of at least ≥ 2 biological replicates with each biological replicate comprised of ≥ 2 technical replicates.

Table S5. Top hits from isothermal TPP with DMU371.

Hit	Abundance		Peptides	Gene ID	Protein
	Log ₂ fold change				
	Rep 1	Rep 2			
1	2.50	2.97	22	C4B63_45g239	Lysyl-tRNA synthetase 1 (KRS1)
2	3.04	1.56	4	C4B63_42g593	Small nuclear ribonucleoprotein Sm-E
3	2.05	1.61	4	C4B63_49g169	Conserved hypothetical protein

Table S6. Top hits from isothermal TPP with DMU759. A total of 2365 proteins were detected by the presence of >2 peptides in two replicates. Those with a 1.5-log₂ fold abundance change in both replicates are listed below.

Hit	Abundance		Peptides	Gene ID	Protein
	Log ₂ fold change				
	Rep 1	Rep 2			
1	2.26	1.94	23	C4B63_45g239	Lysyl-tRNA synthetase 1 (KRS1)
2	-2.64	-3.79	9	C4B63_14g170	19S proteasome regulatory subunit
3	-2.04	-2.35	6	C4B63_3g1101	Mitochondrial processing peptidase, beta subunit
4	-2.27	-1.74	9	C4B63_116g3	P-type H ⁺ -ATPase
5	-2.25	-1.75	5	C4B63_42g251	Conserved hypothetical protein
6	-1.59	-1.80	5	C4B63_6g2300	Ribosomal protein S26
7	-1.58	-2.80	8	C4B63_22g162	cysteine peptidase, Clan CA, family C2

Table S7: Statistics for the crystal structure of *TcCpKRS1* with bound DMU371 and lysine.

Beamline	Diamond I04
Detector	DECTRIS EIGER2 XE 16M
Wavelength (Å)	0.95373
Space group	<i>P22₁2₁</i>
Unit cell lengths (<i>a</i> , <i>b</i> , <i>c</i> Å)	73.14, 116.70, 142.88
Unit cell angles (α , β , γ °)	90, 90, 90
Resolution range (Å)	58.42 – 1.60 (1.64 – 1.60)
Total no. of reflections	2111816 (62276)
Total unique reflections	160925 (7506)
Redundancy	13.1 (8.3)
Completeness	99.9 (95.0)
R_{sym}	0.082 (1.212)
R_{pim}	0.033 (0.635)
$\langle I \rangle / \langle \sigma \rangle$	16.0 (1.6)
CC _{1/2}	0.999 (0.628)
R _{work} / R _{free}	18.43 (20.85)
B-factors	
Protein (A/B)	24.1 / 25.3
Ligand (A/B)	22.3 / 21.7
Lysine (A/B)	17.9 / 18.9
Waters	29.9
R.m.s. deviations	
Bond lengths (Å)	0.0111
Bond angles (°)	1.664
Ramachandran favoured / allowed / disallowed (% , all chains)	98 / 2 / 0
PDB code	8s0v

Table S8. Primers used in this study.

Primer	Sequence (5'-3')
G00	AAAAGCACC GACTCGGTGCCACTTTTCAAGTTGATAACGGAC TAGCCTTATTTTAACTTGCTATTTCTAGCTCTAAAAC
JD081	TTAATTAAGCTTATGTCGGCTGTGGAGGAGCTCCGAGC
JD082	TGGGCAGGATCCTCAAAGAAGTGGCACCC
JD085	ACCTGCGAATTGCACCGG
KRS2-qPCR-Rev	TTGAGGGTCATTACGGTGCC
LBT 074	CAATGATAGAGTGGTACCC
LBT 075	TTACTCCGGGAACCTTTC
LBT 082	CTAGTGAGGCGTGCAAATCC
LBT 083	CGTTGACCCTTTTCCTGCAA
LBT 084	ACATCGACCAGTCCAAGTTCG
LBT 094	TTAATAAGATCTATGTCGTCCTCGAAGAGCTCCGTAAGC
LBT 095	TTAATAAGATCTCTACAGCAGGGGAACACCCTGACC
LBT 114	TCGACCTGACCCACAACCCCGAATTTACGNNNTGCGAAGCGTA CTGGGCATACATGGACTACC
LBT 115	GAAATTAATACGACTCACTATAGGCCCCGAATTCACAAGCTGC GGTTTTAGAGCTAGAAATAGC
LBT 148	ACCTCACACACAACCCGGAGTTTACCTTAGTAGAGGCGTACTG GGCCTACGCCGACT
LBT 165	TGTACCTGCGCATTGCTCCC
LBT 166	TGTACGCGTTGCAGAGCTCC
LBT 175	AGTCTGCGTACGCCAATAACTCTCAACAAGTGTGAACTCCGG ATTATGCGTGAGAT
pIR1-SAT-BglII-SeqF	TCATTGCTTCCTTCTGTTCCCTCG
pIR1-SAT-BglII-SeqR	TGGTCGTAGAAATCAGCCAGTACAT
pTREX-F	CATTTTCACGCACGAAAGCG
pTREX-R	CTCGAGCCATTTACGAC